Check for updates

The role of fire in the coevolution of soils and temperate forests

Assaf Inbar*, Petter Nyman, Patrick N.J. Lane and Gary J. Sheridan

[1]School of Ecosystem and Forest Sciences, Faculty of Science, The University of Melbourne

*Corresponding author: Assaf Inbar (assaf.inbar@unimelb.edu.au)

Key Points:

- Wildfire strongly influences forest hydro-geomorphology, yet its net effect on coevolution of soil-vegetation systems is not yet constrained
- We used a new numerical model to test the hypothesis that fire is central to coevolution of forest-soil systems in SE Australia
- The hypothesis was supported and the role of fire was found to increase with aridity due to higher fire frequency and less developed soils

Author Manuscript

This is the author manuscript accepted for publication and has undergone full peer review but has not been through the copyediting, typesetting, pagination and proofreading process, which may lead to differences between this version and the Version of Record. Please cite this article as doi: 10.1029/2019WR026005

This article is protected by copyright. All rights reserved.

Abstract

Climate drives the coevolution of vegetation and the soil that supports it. Wildfire dramatically affects many key eco-hydro-geomorphic processes but its potential role in coevolution of soil-forest systems has been largely overlooked. The steep landscapes of southeastern Australia provide an excellent natural laboratory to study the role of fire in the coevolution of soil and forests, as they are characterized by temperate forest types, fire frequencies and soil depths that vary systematically with aridity. The aims of this study were to i) test the hypothesis that in Southeastern Australia, fire-related processes are critical to explain the variations in coevolved soil-forest system states across an aridity gradient, and ii) to identify the key processes and iii) feedbacks, involved. To achieve these aims we developed a numerical model that simulates the coevolution of soil-forest systems which employ eco-hydro-geomorphic processes that are typical of the flammable forests of Southeastern Australia. A stepwise model evaluation, using measurements and published data, confirms the robustness of the model to simulate eco-hydro-geomorphic processes across the aridity gradient. Simulations that included fire replicated patterns of observed soil depth and forest cover across an aridity gradient, supporting our hypothesis. The contribution of fire to coevolution increased in magnitude with aridity, mainly due to the higher fire frequency and lower post-fire infiltration capacity, increasing the rates of fire-related surface runoff and erosion. Our results show that critical feedbacks between soil depth, vegetation and fire frequency dictates the trajectory and pace of the coevolution of flammable temperate forests and soils.

1 Introduction

Interactions and feedbacks between soil and vegetation are key factors in controlling catchment eco-hydrological behavior (Donohue et al., 2007, 2012; Trancoso et al., 2016; Zhang et al., 2004). Thus, understanding how soil-vegetation systems coevolve can help explain observed variations in catchment responses and enable better predictions of change in response to future climate scenarios (Troch et al., 2015). Coevolution in this context is defined as a climatically-driven process in which interactions and feedbacks between vegetation and its supporting soil causes ongoing changes in their properties (Berry et al., 2005; Porder, 2014; Troch et al., 2015; van Breemen, 1993). Due to its interdisciplinarity, complexity and nonlinearity and because it operates outside of our observational timescales, studying the coevolution of soil-vegetation systems require models that couple ecological, hydrological and geomorphological processes and their drivers under one numerical framework (Istanbulluoglu, 2016).

Fire affects both vegetation and soil, and therefore likely to play a role in their coevolution. Fire changes the hydrological properties of the system by removing the canopy cover and changing the properties of the soil surface (DeBano, 2000; Inbar et al., 2014; Shakesby & Doerr, 2006), often making it more conducive to surface runoff (Nyman et al., 2010; Shakesby & Doerr, 2006) and more erodible (Noske et al., 2016; Nyman et al., 2013). These combined transient effects often result in a temporary increase in soil erosion of different magnitudes (Lane et al., 2006; Moody & Martin, 2001; Nyman et al., 2011; Prosser & Williams, 1998). Fire had also been shown to cause transient changes in the water and energy balance by altering the amount of water that infiltrates, intercepted and transpired by the local forested systems (e.g., Nolan et al., 2014).

The role of fire in coevolution had been mainly investigated through its geomorphic effect on landform change (Benda & Dunne, 1997; Gabet & Dunne, 2003; Istanbulluoglu et al., 2004;

This article is protected by copyright. All rights reserved.

Author Manuscript

Istanbulluoglu & Bras, 2005; Orem & Pelletier, 2016; Roering & Gerber, 2005). Here we point to an important feedback that is indirectly related to the geomorphic effects of fire that might have been overlooked. Soil depth holds an important role in controlling vegetation water holding capacity at a point by setting an upper limit to the plant available water capacity (Hahm et al., 2019). This implies that fire-driven erosion processes could potentially push soil-vegetation systems towards an alternative coevolved state by affecting its soil depth, if high fire-frequency is sustained over long timescales. Accounting for the processes that affect fire frequency is therefore necessary to fully untangle the role of fire in the development of the critical zone and landscape evolution.

In the landscape evolution literature, fire is often regarded as a "disturbance" and is modelled stochastically (Gabet & Dunne, 2003; Istanbulluoglu et al., 2004; Istanbulluoglu & Bras, 2005). However, evidence show that long-term fire frequency depends on processes that control the availability of burnable fuel (Pausas & Bradstock, 2007) and their moisture state (Pausas & Bradstock, 2007; Taufik et al., 2017), making it a dynamic process that is coupled to the ecohydrological state of soil-vegetation systems. This implies that fire is tightly coupled within coevolutionary feedbacks both as a forcing and as a response variable. The modelling of a fire regime that is coupled to the hydrological state of the modelled systems has been explored in some dynamics vegetation models (e.g., Gerten et al., 2004; Prentice et al., 2011; Thonicke et al., 2001, 2010; Yue et al., 2014). These models, however, do not include the geomorphic effect of fire and its consequences on processes and feedbacks in the coevolution of soil-vegetation systems. The full range of mechanisms by which fire can drive landscape change and coevolution is therefore unclear. To address this limitation, a model is required that couples fire to both ecohydrological and geomorphic processes and enables the complex coevolution of vegetation and soil to be more robustly investigated.

The central highlands in southeastern (SE) Australia provide an ideal natural laboratory to investigate the role of fire in coevolution of soil-vegetation systems for several reasons: (i) it is home to some of the most flammable forests on earth; (ii) a gradient in temperate climate had resulted in a range of forest types with different fire regime (Cheal, 2010); (iii) the lack of active uplift (Czarnota et al., 2014; Wellman, 1987) and the lack of glaciation below 1200 m elevation during late Pleistocene (Barrows et al., 2001) narrows down the drivers and possible geomorphic processes that might have affected coevolution in the area.

The aims of this study were to i) test the hypothesis that fire-related processes are critical to explain the variations in coevolved soil-forest systems across an aridity gradient in SE Australia, and ii) to identify key processes, and iii) feedbacks, involved the coevolution process. To achieve the aims we developed a numerical model (COevOLution of FLAMmable Systems - CoolFlameS) that simulates the coevolution of soil-forest systems, and is underpinned by equations that couple fundamental ecohydrological, vegetation dynamics and geomorphological processes. CoolFlameS was formulated, parameterized and calibrated to simulate systems that are typical to SE Australia. The model was evaluated by comparing model outputs of system properties and process rates against observations, measurements and published data.

This paper:

1. describes the conceptual framework and model development;
2. reports the results of model verification with field data;

This article is protected by copyright. All rights reserved.

3. evaluates the hypothesis and identifies interactions and feedbacks that are involved in the coevolution process.

2 Regional description and scope

The study focuses on the southern part of the Great Dividing Range, Victoria, Australia, which consists of a mix of plateaus, ridges and dissected uplands with elevations ranging from 200 to 2,000 m above sea level. Geology is dominated by Paleozoic marine sedimentary rocks, with some regional igneous plutons (mainly granite and granodiorite). After peaking in late Cenozoic, uplift is now believed to be limited mainly to isostatic rebound (Czarnota et al., 2014; Wellman, 1987). Climate in the region is temperate, characterized by warm, dry summers, and cool, wet winters (Stern et al., 2000). Mean seasonal temperatures range from 13.4 and -1.1 °C in winter and 25.8 to 17.6 °C in summer, for low and high elevations, respectively. Mean annual precipitation (MAP) range from 600 to 2,500 mm yr^{-1} for low and high elevations, respectively. Interannual variability in rainfall is mainly driven by Southern Annular Mode, El Niño-Southern Oscillation, Inter-decadal Pacific Oscillation and Indian Ocean Dipole (Timbal et al., 2016).

The temperate forests of SE Australia are dominated by *Eucalyptus* spp., most of which are highly adapted to drought and fire (Specht & Wood, 1972). At low-intermediate elevations (200-1200m above sea level), forests range from productive, tall eucalyptus forests (Keith et al., 2009) at locations with a MAP of 1200-2000 mm yr^{-1} to less-productive dry eucalyptus forests and woodlands in areas with a MAP of 600-1000 mm yr^{-1} (Cheal, 2010). Across these productive temperate forests, fuel is abundant and the frequency of medium-high severity fire (ranging from 10-150 years (Cheal, 2010)) is largely controlled by moisture (Bradstock, 2010; Krawchuk & Moritz, 2011; Nyman et al., 2018) rather than fuel quantity.

The effects of wildfire on eco-hydro-geomorphic processes in the region has been the focus of many studies (e.g., Cawson et al., 2012; Kuczera, 1987; Lane et al., 2004; Nolan et al., 2014; Noske et al., 2016; Nyman et al., 2011, 2013, 2019; Sheridan et al., 2007, 2015; Van der Sant et al., 2018; Vertessy et al., 2001). Recent studies identified that the sensitivity of the soil to post-fire erosion increases nonlinearly with aridity due to the magnitude of post-fire reduction in hydraulic conductivity at the soil surface (Noske et al., 2016; Sheridan et al., 2015; Van der Sant et al., 2018). The combined effect of the differences in forest type, fire frequency, soil properties and post-fire surface runoff response creates a gradient in the severity of erosion events across the aridity spectrum (Noske et al., 2016; Sheridan et al., 2015), from negligible in the low aridity forests (Lane et al., 2004; Sheridan et al., 2007) to severe in the more arid ones (Noske et al., 2016; Nyman et al., 2011).

3 Numerical model

3.1 Model description

In systems where nutrient availability is not limiting plant growth, vegetation carrying capacity is driven by the supply and demand for water and the ability of the critical zone to store it (Hahm et al., 2019). While water supply and demand are often affected by climate and topography (Nyman et al., 2014b; Rasmussen et al., 2015), the ability of a system to store water depends on soil properties, primarily depth, but also texture, porosity, and organic matter content (Clapp & Hornberger, 1978; Saxton & Rawls, 2006). CoolFlameS is therefore based on the conceptual model whereby the structure of soil-forest systems at any point in time and space is controlled by

Author Manuscript

This article is protected by copyright. All rights reserved.

the legacy of climatically driven feedbacks between vegetation, fire and the ability of the system to hold moisture, which is dictated by soil depth (Hahm et al., 2019). In the proposed model (Figure 1a) soil moisture plays a central role in coevolution by controlling evapotranspiration and primary productivity (Montaldo et al., 2005; Rodriguez-Iturbe, 2000) and by ecohydrological control on the flammability of the system (Krueger et al., 2016). Soil water holding capacity in the model is determined primarily by soil depth, and together with climate (i.e., aridity), limits evapotranspiration and biomass accumulation (Klein et al., 2015; Milodowski et al., 2015). Fire removes vegetation and causes changes to soil hydraulic properties (Certini, 2005; DeBano, 2000), which temporarily increases erosion potential (Nyman et al., 2013; Wagenbrenner et al., 2010). By this approach, changes in climate and fire frequency can alter the depth of the soil, its water and biomass holding capacity, and thereby drive coevolution.

In order to investigate the role of fire in the coevolution of soil-vegetation systems, it is necessary to couple fire with ecological, ecohydrological and geomorphic processes. One of CoolFlameS major novelty is that it bridges the gap between landscape evolution, land surface models and flammability through coupling ecohydrology, vegetation dynamics and moisture deficits with geomorphic processes that control soil depth. This feature is missing from existing models. For this purpose, we employ a combination of new and well-established generic equations that represent ecohydrological, geomorphological and forest dynamics processes as defined in existing literature. Moreover, in order to represent SE Australian systems appropriately, CoolFlameS was developed from deep ecohydrological and geomorphic understanding stemming from decades of intensive research and model development. Due to the long-timescale and multitude of disciplines and processes involved in the coevolution of soil-vegetation systems, simplicity was prioritized over complexity during model development. To overcome this potential shortcoming, model components (i.e., ecohydrology, geomorphology and fire) were evaluated by comparing simulation results with measurements and published values.

3.2 Model Formulation

In this section, existing generic equations are described in short. Where appropriate, the reader is directed to the existing literature for additional information. In case new or modification to generic equations is introduced, more detailed description and reasoning are added. In some cases, the reader is referred to the Supporting Information supplement for additional information regarding specific model components. Model parameter values are described in Table 1.

CoolFlameS, which is inspired by work of others (eg., Istanbulluoglu & Bras, 2006; Yetemen et al., 2015; Zhou et al., 2013), couples ecohydrological and geomorphological processes to drive coevolution by numerically solving a set of ordinary differential equations for surface energy, soil moisture, biomass and soil depth (Istanbulluoglu, 2016):

Energy:
$$\frac{dS_h}{dt} = R_{net} - G - H_s - \lambda ET \quad (1)$$

Soil moisture:
$$nH\frac{ds}{dt} = I - ET - D \quad (2)$$

This article is protected by copyright. All rights reserved.

Biomass: $$\frac{d\mathrm{B}}{dt} = NPP - B(f_F\, b_{mort} + k_b) \quad (3)$$

Soil depth: $$\frac{dH}{dt} = \frac{\rho_r}{\rho_s}\varepsilon - (E_F + E_D) \quad (4)$$

Change in surface heat storage dS_h (MJ m^{-2}) with time, t (day) (Eqn. 1), is the difference between net solar radiation (R_{net}; MJ m^{-2} d^{-1}) and ground (G; MJ m^{-2} d^{-1}), sensible (H_s; MJ m^{-2} d^{-1}) and latent (λET; where λ is latent heat of vaporisation and ET is evapotranspiration; MJ m^{-2} d^{-1}) heat fluxes (Istanbulluoglu, 2016).

Daily change in soil moisture (mm d^{-1}; where s is relative soil saturation; n is soil porosity; and H is soil depth, respectively; Eqn. 2) is the balance between the rate of infiltrated water (I; mm d^{-1}), ET (mm d^{-1}) and deep drainage (D; mm d^{-1}).

Change in standing biomass density (as dry mass), B, (kg m^{-2} d^{-1}; Eqn. 3) is the difference between net primary production (NPP; kg m^{-2} d^{-1}) and the processes that remove biomass, simplified here as senescence and combustion. In simple terms, combustion is modelled using fire frequency (f_F; d^{-1}) and the mean proportion of biomass that is removed by each fire, b_{mort}. Similar to other models (Williams & Albertson, 2005; Yetemen et al., 2015; Zhou et al., 2013), senescence coefficient (k_b) includes within it various ecological processes from self-thinning to seasonal LAI response. k_b is modelled here as a function of the recovery state of the vegetation as will be described below.

Change in soil depth, H (m yr^{-1}; Eqn. 4), is modelled as the balance between the rate of soil production (ε) and erosion (E; m yr^{-1}). For simplicity, we assume that soil is produced directly from bedrock to transportable minerals without intermediate conversion to saprolite (Brantley et al., 2017). Downslope transport of sediment includes diffusive- and advective- (or fluvial) processes (eg., Dietrich et al., 2003; Tucker & Hancock, 2010) denoted here by the terms E_D and E_F, respectively. While advective processes occur at the soil surface, both ε and E_D depend on H to account for the depth to disturbance at the bedrock interface (Heimsath et al., 1997; Roering, 2008). ρ_r and ρ_s in equation 4 are rock and soil densities (kg m^{-3}), respectively.

Figure 1b illustrates the way in which ecohydrological and geomorphological processes and fire are represented and coupled in the model. Rainfall is partitioned by the canopy and at the soil surface. Daily potential evapotranspiration evaporates water from the canopy and soil surface and drives the coupled transpiration-primary production process (e.g., Williams & Albertson, 2005). To represent a dynamically coupled fire cycle, stand flammability is linked to cumulative soil moisture deficit (Krueger et al., 2016), which is directly affected by the annual water balance. Stochastic fires remove a proportion of the vegetation and change the sediment availability and hydrological properties of the soil surface, all of which have been shown to cause an increase in overland flow and fluvial erosion (Noske et al., 2016; Van der Sant et al., 2018).

Author Manuscript

This article is protected by copyright. All rights reserved.

3.2.1 Land surface representation

CoolFlameS simulates the evolution of a hypothetical point on a hillslope located 50m downslope from the ridgetop. This drainage position was chosen in order to avoid modelling the complex erosion-deposition balance (Patton et al., 2018) and substantial water subsidies further down in the convergent zone (Western et al., 1999), while still maintaining the potential effect of topographic aspect on the energy balance (Rasmussen et al., 2015). For simplicity, inflow of subsurface water from the ridgetop is assumed negligible.

Similar to other models (Williams & Albertson, 2005; Yetemen et al., 2015; Zhou et al., 2013), the modelled land surface is proportionally divided horizontally between vegetated and unvegetated surface areas (Figure 1c). The horizontal division is computed dynamically using modelled leaf area index (LAI_l) and is used to partition fluxes of energy (expressed here as E_P) and rainfall at the canopy level. Partitioning of a given flux by the forest canopy is modelled using two dynamic variables: vegetation cover, V_C and the leaf area index ratio of the covered fraction, LAI_r. These dynamic variables are calculated using:

$$V_C = \frac{LAI_l}{LAI_{gmax}} \tag{5a}$$

$$LAI_r = \frac{LAI_l}{LAI_{lmax}} \tag{5b}$$

where LAI_{gmax} and LAI_{lmax} are the maximum potential LAI in SE Australia and the maximum potential LAI for a given set of edaphic and climatic conditions (i.e., long-term aridity and soil depth), respectively. Using this approach V_C represents the proportion of area that is covered by vegetation and $(1 - V_C)$ represents bare proportion (Williams & Albertson, 2005; Yetemen et al., 2015; Zhou et al., 2013). LAI_r represents the recovery state of the LAI within the vegetated surface area (V_C). $LAI_r < 1$ indicates that the canopy of the vegetated surface area has not yet reached its full cover potential.

3.2.2 Climatic forcing

In the model, evapotranspiration, biomass balance and background geomorphic processes run on daily timesteps. During rainstorms, however, the model is forced with hourly rainfall, and hydrological and geomorphological processes are simulated on an hourly timestep. This transition is necessary in order to better represent infiltration excess, runoff generation and soil erosion processes that are better represented on sub-daily timesteps.

In order to simplify the energy balance, interterm changes in S_h are assumed negligible ($dS_h/dt = 0$) thus allowing the model to be driven by potential evapotranspiration (E_p; mm d^{-1})(Yetemen et al., 2015). During model simulations, daily E_p is applied using a cosine function following Small (2005):

Author Manuscript

This article is protected by copyright. All rights reserved.

$$E_p(DOY) = \frac{\Delta d}{2} cos\left[2\pi\left(\frac{DOY - L_T - {N_d}/{2}}{N_d}\right)\right] + E_{p-daily} \quad (6)$$

where DOY is day of the year; Δd (mm d^{-1}) is the difference between maximum and minimum values of daily E_p; L_T is the lag (in days) between peak E_p and peak solar forcing; N_d is number of days in a year (set to 365 assuming no leap years); and $E_{p-daily}$ is mean annual daily E_p (mm d^{-1}). Values for Δd and $E_{p-daily}$ were obtained by calculating monthly E_p with R_{net} and T_a data using the Priestly-Taylor equation (Priestley & Taylor, 1972):

$$E_p = 1.26\frac{\Delta}{(\Delta + \gamma)}(R_{net} - G) \quad (7)$$

where Δ is the slope of the saturation vapor pressure (kPa $^oC^{-1}$), which is a function of T_a; and γ is psychrometric constant (kPa $^oC^{-1}$). On daily timesteps, G from a vegetated surface can be 1-2 orders of magnitude smaller than the other heat fluxes in the surface energy balance (Brutsaert, 1982) and was thus neglected in the calculation of E_p (Eqn. 7).

On days with rainfall, a Poisson-shaped hourly rainfall (p, mm h^{-1}) is applied using a single-site Neyman-Scott Rectangular Pulse (NSRP) model (Cowpertwait et al., 1996). For this purpose, NSRP model simulator (Camici et al., 2011; Tarpanelli et al., 2012) was calibrated using existing long-term hourly rainfall records, as is described in Text S1.

3.2.3 Ecohydrology

Ecohydrology in CoolFlameS employs an ensemble of new and modified published equations and novel approaches to solve equation 2 by partitioning rainfall and energy (represented as E_p) across the land surface on a daily basis. On days with rainfall, however, equation 2 is solved by aggregating processes during 24-hours.

Rainfall interception

Rainfall interception is modelled as a simple bucket-type model with a probability distribution approach (Kandel et al., 2005) to account for rainfall intensity. Here we use a two-step method to model actual interception (C_a; mm h^{-1}) and actual throughfall (P_{thr}; mm h^{-1}). First, we use we use modelled leaf area index (LAI_l) to spatially partition the hourly rainfall into the portion that: (i) falls directly over the vegetated surface (P_V; mm h^{-1}); and (ii) reaches the soil surface by passing through the leaves, branches and trees (P_B; mm h^{-1})(Figure S1). In the second step P_V is temporally partitioned to account for rainfall intensity on interception. P_V and P_B can be then calculated using:

$$P_V = p\, V_C LAI_r \quad (8a)$$

$$P_B = p\,[1 - V_C LAI_r] \quad (8b)$$

This article is protected by copyright. All rights reserved.

Author Manuscript

CoolFlameS tracks actual canopy moisture storage c_o, defined as the proportion of the canopy water holding capacity (C_{cap}; mm) that is occupied by water ($1 \geq c_o \geq 0$). C_{cap} is calculated using $C_{cap} = S_{LAI}\, LAI_l$, where S_{LAI} (mm LAI^{-1}) is the amount of water that the can be stored for a given unit leaf area (Table 1). S_{LAI}, was calibrated using achieving around 20% interception loss (as a proportion of rainfall) under the wettest climatic scenario, assuming it resembles a mature wet Eucalyptus regnans forest (Vertessy et al., 2001). C_a and P_{thr} are then calculated using:

$$C_a = c_{prop}\, P_V \tag{9a}$$

$$P_{thr} = P_B + P_V\left(1 - c_{prop}\right) \tag{9b}$$

where c_{prop} (-) is the proportion of the rainfall that is intercepted and remains the canopy (Eqn. S2). To account for rainfall intensity in the interception process, c_{prop} is computed using a probability distribution approach, assuming that the hourly rainfall is exponentially distributed (Kandel et al., 2005). In the approach, c_{prop} is calculated by using the Cumulative Distribution Function of P_V, with the available canopy water stores (C_f) as a cut-off value (P_V; Eqn. 8a). Text S2 in the Supplementary information provides additional information with regards to the way the probability distribution approach is used to calculate c_{prop}.

Infiltration and surface runoff

A simple conceptual representation of water movement into and within the soil profile is employed in order to model the partitioning of throughfall at the soil surface. In this concept, the movement of water into the soil is controlled by a competition between its capacity to allow infiltration and its ability to allow water movement within it. I_p is calculated using:

$$I_P = \min(I_c, K_s) \tag{10}$$

where I_p is infiltration potential; I_c is infiltration capacity; and K_s is saturated hydraulic conductivity (all in mm h^{-1}). The partitioning of throughfall (P_{thr}) into actual infiltration (I_a; mm h^{-1}) and surface runoff (Q; mm h^{-1}) is computed using a probability distribution approach, similar to the method used in the partitioning of hourly rainfall in the interception process (Kandel et al., 2005). I_a and Q are calculated using:

$$I_a = min\left(i_{inf} P_{thr}, s_E\right) \tag{11a}$$

$$\mathrm{Q} = P_{thr} - I_a \tag{11b}$$

where i_{inf} is the proportion of P_{thr} that infiltrates through the soil surface; and s_E (mm) is the actual pore volume that is left in the soil profile to accommodate the infiltrating water, calculated using: $s_E = (1 - s)nH$. i_{inf} is calculated using the Cumulative Distribution Function of P_{thr}, with I_p as a cut-off value (Eqn. S3). Text S2 in the Supplementary information provides

This article is protected by copyright. All rights reserved.

additional information with regards to the way the probability distribution approach is used to calculate i_{inf}.

Evapotranspiration

Actual evapotranspiration rate (ET_a; mm d^{-1}) is modelled following Rodriguez-Iturbe et al. (1999a) and Laio et al., (2001). A few modifications had been done to the employed approach to account for the partitioning of energy across the modelled land surface.

In this approach, which was used in several other models (Istanbulluoglu & Bras, 2006; Yetemen et al., 2015; Zhou et al., 2013) ET_a is scaled between zero and maximum possible daily ET (ET_{max}, mm h^{-1}) using available soil moisture. We assume that the available energy is first used to evaporate water that was intercepted by the canopy. ET_{max} is therefore modelled by partitioning the remainder of the available energy ($E_p - E_i$; where E_i is the rate of interception loss in mm d^{-1}) into maximum transpiration (T_{max}) and maximum soil evaporation (E_{max}) across the land surface (using V_c and LAI_r).

$$ET_{max} = T_{max} + E_{\max} \tag{12a}$$

$$T_{max} = [E_p - E_i]\, V_c\, LAI_r \tag{12b}$$

$$E_{max} = E_s[E_p - E_i][1 - V_c\, LAI_r] \tag{12c}$$

where E_s reduces E_p to achieve maximum soil evaporation (Istanbulluoglu et al., 2012; Zhou et al., 2013). Evaporation rate of intercepted water, E_i, is calculated using:

$$E_i = min(\, E_p\, , C_o C_{cap}) \tag{13}$$

Once ET_{max} is calculated, actual evaporation, ET_a, is then computed using:

$$ET_a = ET_{max}\, \beta(s) \tag{14a}$$

$$\beta(s) = \begin{cases} 0 & s \le s_h \\ E_w \dfrac{s - s_h}{s_w - s_h} & s_h < s \le s_w \\ \dfrac{s - s_w}{s_i - s_w} & s_w < s \le s_i \\ 1 & s > s_i \end{cases} \tag{14b}$$

where β is the evapotranspiration efficiency term that scales nonlinearly across the plant available water capacity continuum; and $s_h, s_w, s_{fc,}$ and s_i are degree of saturation at hygroscopic capacity, wilting point, field capacity and incipient stomata closure (defined as the degree of saturation value below which vegetation start to close their stomata due to water stress), respectively (Laio et al., 2001; Rodriguez-Iturbe et al., 1999b); and E_w is an evaporation scalar for conditions when s is under wilting point, and has the value of 0.1 (Laio et al., 2001; Rodriguez-Iturbe et al., 1999b). Values for s_h, s_w and s_{fc} are for clay loam soil (Clapp & Hornberger, 1978), which is on average the dominant soil type in the model domain (Rees, 1982). The value for s_i was estimated to be between s_{fc} and s_w (Table 1).

This article is protected by copyright. All rights reserved.

In order to represent and simplify plant available water dynamics in the model, the following assumptions were made: (i) soil properties are homogenous throughout the soil profile and readily accessible to plant roots (ii) subsurface inflows from upslope are considered negligible; (iii); the excess soil moisture drains vertically and is lost via deep drainage, which only occurs when s is above field capacity: $s_{fc} < s \leq 1$. By keeping other soil hydrological properties constant, plant available water capacity is dictated solely by soil depth.

Finally, deep drainage, D (mm h^{-1}), is modelled as a simple function that incorporates available soil moisture and saturated hydraulic conductivity (K_s; mm h^{-1}), following Zhou et al. (2013).

$$D(s) = K_s \, s^{(2b_{ret}+3)} \tag{15}$$

where b_{ret} is a water retention parameter (Table 1).

3.2.4 Biomass balance

Biomass balance is modelled similar to Williams and Albertson (2005) and Zhou et al. (2013). In this model, biomass balance (Eqn. 3) is coupled to the energy (Eqn. 1) and soil moisture (Eqn. 2) dynamics through the effect of ET on gross primary production (GPP). Some modifications to the existing biomass balance model were implemented to account for: (i) the different representation of the land surface; (ii) the initiation of post-fire recovery; and (iii) limits of biomass accumulation at a point.

Daily net primary production (kg m^{-2} d^{-1}) is coupled to plant transpiration (T_a; mm h^{-1}), and is modelled as the difference between gross primary production and autotrophic respiration Following Zhou et al. (2013):

$$NPP = \mu \, T_a \, WUE \, \rho_w \, \omega \tag{16}$$

where μ is the ratio between NPP/GPP (Waring et al., 1998); WUE is water use efficiency ($kg_{CO_2} \; kg_{H_2O}{}^{-1}$); ω is the conversion ratio of CO_2 to dry matter ($kg_{DM} \; kg_{CO_2}{}^{-1}$) and ρ_w is density of water (kg m^{-3}). T_a is calculated as a proportion of actual ET using $T_a = T_{max}/ET_{max} \, ET_a$. For simplicity, all tree functional groups throughout the domain are assumed to be comprised from the Eucalyptus genera and share the same carbon assimilation traits.

Similar to Williams and Albertson (2005) and Zhou et al. (2013), B is divided into leaf (B_l) and structural (B_s; which includes stem and root biomass) biomass pools. Using their approach, daily NPP (Eqn. 16) is partitioned between B_l and B_s using a simple allocation coefficient Φ, which depends on the state of LAI_l relative to its maximum potential state (calculated using $\Phi = [1 - (LAI_l/LAI_{lmax})]$). LAI_l is calculated daily using $LAI_l = B_l \, SLA$, where SLA (LAI kg^{-1}) is specific leaf area (Table 1).

Daily rate of change in B_l and B_s are modelled daily using the following ordinary differential equations:

$$\frac{dB_l}{dt} = \Phi NPP + k_R B_{lmax} - k_{sl} B_l \tag{17a}$$

This article is protected by copyright. All rights reserved.

$$\frac{dB_s}{dt} = (1 - \Phi)\, NPP - k_{ss} B_s \tag{17b}$$

where k_{sl} and k_{ss} are leaf and structural biomass turnover coefficient (d^{-1}); k_R is the leaf biomass accumulation rate factor that initiates and propagates B_l recovery during the first year after a fire (d^{-1}). Forest and vegetation dynamic processes such as self-thinning and wind breakage are implicitly represented in the coefficient k_{ss}.

In order to constrain the accumulation of biomass and to prioritize positive biomass increments during post-fire recovery, a logistic function for k_{ss} was introduced:

$$k_{ss}\left(\frac{B_s}{B_{smax}}\right) = \left(\frac{k_{ssmax}}{1 + exp^{-a_{kss}\left(\frac{B_s}{B_{smax}} - c_{kss}\right)}}\right) \tag{18}$$

where B_{smax} is the maximum structural biomass holding capacity at a point; and a_{kss} and c_{kss} are coefficients that were calibrated to achieve the regeneration of 90% of B_{max}within ~200 years (Keith et al., 2014) under wet climatic scenarios. The variable k_{ssmax} represents the maximum possible value for k_{ss}, and is calculated using $k_{ssmax} = NPP(1 - \Phi)/B_{smax}$ assuming that: (i) maximum turnover is reached when structural biomass had reached steady-state conditions (i.e., $dB_s/dt = 0$ and $B_s = B_{smax}$; Eqn. 17b); and that (ii) LAI_l had almost fully recovered ($\Phi \approx 0$).

In CoolFlameS, biomass density at a point is assumed to be constrained by the supply and demand for water and the ability of the coupled soil-vegetation systems to store it. Maximum biomass density, B_{max} (kg m^{-2}), is therefore defined, assuming it decreases exponentially with aridity (i.e., increase in dryness) and increases exponentially with soil depth (i.e., increase in water holding capacity):

$$B_{max} = \alpha_b\left(\, exp^{-m_1 \overline{AI}_{100}}\right)(1 - \, exp^{-m_2 H}) \tag{19}$$

where α_b, m_1 and m_2 (Table 1) are calibrated parameters; and $\overline{AI}_{100}$ is a 100-years mean of annual aridity index calculated using $\overline{AI}_{100} = \overline{E_p}/\overline{P}$ (where $\overline{E_p}$ and $\overline{P}$ are mean annual potential evapotranspiration and rainfall, respectively). The timeframe for calculating $\overline{AI}_{100}$ was chosen to overcome annual fluctuations in climate, which in any case not expected to produce drastic changes in maximum biomass values. Maximum potential LAI values for a given B_{max} is then calculated using the empirical relationship:

$$LAI_{lmax} = LAI_{gmax}(1 - \, exp^{-m_3 B_{max}}) \tag{20}$$

where LAI_{gmax} and m_3 are calibrated parameters. LAI_{gmax} represents the maximum possible LAI in native Eucalyptus forest. LAI_{gmax}, LAI_{gmax} and LAI_l are used to partition the modelled surface area between the vegetated and bare proportions using Eqn. 5a and 5b. B_{max} and LAI_{lmax} are calculated on daily timesteps. Maximum leaf biomass, B_{lmax}, is then calculated using $B_{lmax} = LAI_{lmax}/SLA$, and B_{smax} using $B_{smax} = B_{max} - B_{lmax}$.

This article is protected by copyright. All rights reserved.

Author Manuscript

3.2.5 Soil depth balance

We use a combination of generic, modified and new equations to model the daily change in soil depth (Eqn. 4). The geomorphic processes are represented on a daily timestep, however, fluvial erosion, E_F, which depend on hourly rainfall is summed over 24 hours.

Soil production and hillslope diffusion

A generic exponential function (Heimsath et al., 1997) was chosen to express the rate of soil production, ε (m d^{-1}):

$$\varepsilon = \varepsilon_o \, exp^{-Hcos\,(S_{50})/H^*} \quad (21)$$

where $Hcos\ (S_{50})$ is soil depth normal to the slope at 50 m from the ridgeline, H* is the e-folding depth of the soil production rate; and ε_o is maximum soil production when $H = 0$.

Erosion due to diffusive processes describe gravity-driven movement of sediments such as soil creep, wetting-drying cycles, bioturbation, dry ravel etc. (Dietrich et al., 2003; Gabet et al., 2003; Roering et al., 1999, 2010). Soil erosion due to hillslope diffusion is modelled using a generic equation that describes the nonlinear, depth-dependent diffusive sediment flux (q_d; m^2 d^{-1}), following Roering (2008):

$$q_d = -\frac{K_c\, S}{1 - \left(\frac{S}{S_c}\right)^2} \quad (22)$$

where S_c is the angle of repose; S is hillslope gradient; and K_c (m^2 d^{-1}) is a constant that scales non-linearly with soil depth, calculated using $K_c(H) = \eta(1 - exp^{-\beta_r H})$, where η and β_r are calibrated constants (Roering, 2008). Net soil loss from these processes, E_D, is modelled by calculating the difference between incoming and outgoing q_d values for a pixel that its center is at 50m down from the ridgeline. A Detailed description for calculating E_D is presented in Text S3.

Fluvial processes

Fluvial erosion depends on soil erodibility, which in an unburnt state is assumed to be uniform with depth. Studies from SE Australia have shown that after a severe wildfire the top part of the soil loses its cohesiveness and immediately becomes highly erodible (Nyman et al., 2011; Smith et al., 2011b). The loss of cohesiveness was found to be related first and foremost to the combustion of root biomass close to the soil surface (Nyman et al., 2013). Nyman et al. (2013) found that the non-cohesive layer (that consists of mixture of gravel, sediment, ash and wood debris) varies between 7.5-9.1 mm in depth. We therefore conceptually divide soil profile into two distinct layers. We define that all the soil profile is considered cohesive (CO) in its unburnt state. During the first year after a fire, only the top-most layer of soil becomes non-cohesive (NC) overlying a cohesive mantle. Fluvial erosion from CO and NC soil layers are treated differently.

In CoolFlameS fluvial erosion is driven by infiltration excess overland flow (Q) and hence modelled on an hourly basis. We assume that erosion from the CO layer is limited by its erodibility (K_e, h m^{-1}), and therefore classify it as detachment-limited.

This article is protected by copyright. All rights reserved.

Author Manuscript

Hourly detachment limited fluvial erosion rate (E_{FDL}, m h^{-1}) is modelled using a generic equation for calculating the difference between excess and critical shear stress (τ and τ_{crit}, respectively; Eqn. 23). Detachment limited erosion (E_{FDL}, m h^{-1}) is computed using the excess shear stress equation, which is widely used in the geomorphic literature (Istanbulluoglu, 2016; Tucker & Hancock, 2010; Wagenbrenner et al., 2010):

$$E_{FDL} = \frac{K_e[\tau - \tau_{crit}]}{\rho_s} \quad (23)$$

where τ and τ_{crit} (Pa) are boundary and critical shear stress, respectively. τ is calculated using Manning's equation: $\tau = \rho_w\, g\, {n_T}^{n_{st}}\, {q_{60}}^{n_{st}}\, (sin\, S_{50})^{m_{st}}$, where Q_{60} (m^{3}h^{-1}m^{-1}) is discharge at 50 m down the slope; n_{st} and m_{st} are 0.6 and 0.7, respectively; and n_T is manning's roughness (Table 1). Due to lack of empirical evidence from unburnt hillslopes in SE Australia, K_e and τ_{crit} (Table 1) were obtained from values published by Wagenbrenner et al. (2010) from Northwestern United States. The authors reported negative τ_{crit} values in an unburnt state, pointing to little-to-no threshold for the initiation of detachment from unburnt hillslopes during overland flow experiments. Therefore, τ_{crit} value was set to zero (Table 1) for overland flow, making detachment limited erosion solely a function of discharge and the erodibility of the CO soil mantle.

Erosion from the NC layer is assumed to be transport limited (Nyman et al., 2013), depending on the transport capacity of the overland flow and the quantity of available sediment. Post-fire availability of transportable material on hillslopes is not unique to SE Australia (Cannon et al., 2001). Here, however, in order to model transport limited erosion (E_{FTL}, m h^{-1}), we use a combination of generic equations for stream power (Ω; kg m^{-1} h^{-3}) with equations that are more specific to what had been observed in SE Australia (Nyman et al., 2013). The basic equations are presented below. The reader is encouraged to seek additional details in the supplementary information (Text S4).

Transport limited erosion is calculated using (E_{FTL}, m h^{-1}): -

$$E_{FTL} = H_{NC_o}\, h_{pNC} \Omega \quad (24)$$

where H_{NC_o} is the depth (m) of the NC layer; h_{pNC} is the proportion of the NC layer that is eroded per unit time (Eqn. S6); and Ω is the stream-power (kg m^{-1} h^{-3}), calculated using Manning's equation (Text S4). Nyman et al. (2013) found that the removal of the NC layer occurs during short-duration high-intensity rainstorms. We therefore model Ω using the peak 15-minute surface runoff (Q_{15}; mm h^{-1}) by assuming that hourly rainfall is exponentially distributed and that Q_{15} (which is calculated using the 3rd quartile of the hourly runoff) is the result of the most intense 15-minute rainfall within the hour (Text S4; Eqn. S5). For simplicity, we assume that the NC layer prevents detachment limited erosion from occurring until all of it is removed. After the first year following wildfire, all the soil profile regains its cohesiveness and erosion returns to be detachment limited (Nyman et al., 2013).

Author Manuscript

This article is protected by copyright. All rights reserved.

3.2.6 Wildfire and its effects

Flammability

Only high severity wildfires are considered in CoolFlameS due to the minor effects of fires of lower severity on the woody vegetation and soil processes (Prosser & Williams, 1998). Fire occurrence is often modelled as a Poisson or Bernoulli process with either an equal probability of occurring each year (Istanbulluoglu et al., 2004; Istanbulluoglu & Bras, 2005) or as a function of time since last fire (Gabet & Dunne, 2003). Wildfire in Australia's temperate forests is highly correlated with fuel moisture (Bradstock, 2010; Nolan et al., 2016). A simple fire model was therefore developed by coupling the probability of fire to the flammability of the modelled system, which is in turn linked to its annual soil moisture deficit. We consider annual soil moisture deficit to be a reliable indicator for flammability of the system as it represents its long-term cumulative moisture deficit and plant stress (Krueger et al., 2016). Flammability (F_p) is modelled using:

$$F_p = \kappa_f \, s_{pdef} + \delta \tag{25}$$

where s_{pdef} is the cumulative number of days during the previous year that soil moisture was below a certain moisture deficit (or flammability) threshold (s_{cut}); and κ_f and δ are calibration parameters. s_{cut} (Table 1) is calibrated using Average Fire Cycle estimates of typical SE Australian forests based on previous work (Cheal, 2010; Kennedy & Jamieson, 2007). Details of the fire modelling approach and calibration process are given in Text S5. F_p is calculated in summer for every year of simulations whereby a fire occurs whenever it is higher than a random number generated from a uniform distribution.

Post-fire change in infiltration capacity

Aside from changing the cohesiveness of the soil surface (section 3.2.5), fire alters the infiltration capacity of the soil by increasing water repellency (DeBano, 2000). Infiltration capacity, I_c (mm h^{-1}), is calculated annually as a function of long-term aridity ($\overline{AI}_{100}$) and time since fire (Langhans et al., 2016):

$$ln(I_c) = r_{a_{y=i}} \, \overline{AI}_{100} + r_{b_{y=i}} \tag{26}$$

where $r_{a_{y=i}}$ and $r_{b_{y=i}}$ are constants which change depending on the number of years ($y = i$) since the last fire (i.e., first year, second year and unburnt). During model simulations $\overline{AI}_{100}$ is calculated daily and combined with time since fire to calculate I_c. Mean 100-year aridity index is considered here arbitrarily assuming an estimated lag between changes in climate to significant changes in vegetation and soil hydraulic properties. Values for $r_{a_{y=i}}$ and $r_{b_{y=i}}$ parameters were calibrated using a published data from the study area for burnt (Table 2 in Langhans et al., 2016) and unburnt forests as described in Text S6.

Tree mortality and post-fire regeneration

The response of SE Australian temperate forest vegetation to fire can be divided into two main strategies: (i) *"Fire Sensitive" Species*, or "Obligate seeders", that die and regenerate from

This article is protected by copyright. All rights reserved.

Author Manuscript

seed, which dominates forests under damp-wet rainfall regime; and (ii) *"Fire Tolerant" Species*, or "resprouters" that regenerate through resprouting of epicormics shoots, and dominate forests under lower-intermediate rainfall regime (eg., Clarke et al., 2015; Fairman et al., 2016). The two recovery strategies in these forests control the effect of fire and the rate of recovery. Applying a simple approach, it is assumed that the proportion of tree species that are hosted in a given location varies non-linearly with aridity. Using this assumption, every modelled site, depending on its aridity, has different proportions of these two types strategies, which determines the vegetation response to fire (Clarke et al., 2015).

In the model, leaf biomass (B_s) is reset to zero immediately after every fire (assuming all fires are severe) regardless of the type of response. In order to account for fire effects on tree mortality, structural biomass (B_s; Eqn. 17b) is scaled down after each fire using a mortality factor (b_{mort}), which is modelled using:

$$b_{mort} = \begin{cases} 1 & \overline{AI}, < 1 \\ \alpha_{mort}\ \overline{AI}^{\ -\beta_{mort}} & \overline{AI}, \geq 1 \end{cases} \quad (27)$$

where α_{mort} and β_{mort} are calibration parameters (Table 1). The function was parameterized based on local observations and expert opinion depending on estimates of the proportion of fire tolerant species and fire sensitive species across the domain.

In order to initiate recovery, we assume that leave biomass, B_l, is the first to regenerate. Leaf biomass accumulation factor (k_R; Eqn. 17a) is used in this case to initiate the recovery and propagate the rate in which B_l accumulates during the first year after a fire:

$$k_R = f_c \Phi k_{lp} \theta_m \quad (28)$$

where f_c is a Boolean variable that gets the value of 1 only in a year after a fire to activate leaf recovery from seeds or resprout; k_{lp} is leaf production rate (d^{-1}) which is a calibration parameter (Table 1); and θ_m is a modifier that depends on soil moisture, calculated using :

$$\theta_m = \begin{cases} 1 & s \geq s_i \\ \left\{\frac{s - s_w}{s_i - s_w}\right\}^M & s_i > s \geq s_w, \\ 0 & s < s_w \end{cases} \quad (29)$$

where M is a calibrated coefficient (Table 1). Using θ_m in equation 28 allows the leaf biomass regeneration to occur maximum rates when there is sufficient soil moisture, and in lower rates when soil moisture is limited.

3.3 Parametrization and calibration

In order to constrain the model to our defined climo-spatial domain, some of its components were parameterized and calibrated using observations and data from representative field data sites (Inbar et al., 2018; Nyman et al., 2018; Walsh et al., 2017) that vary in rainfall (940-1748 mm yr^{-1}) and aspect orientation (paired north and south facing hillslopes; Figure 2). Details of these sites are elaborated in Text S7 and Table S5 in the supporting information.

In each site, soil depth was measured from soil pits approximately 50m downslope from the ridgeline. Biomass values were estimated by matching observed forest type and structure with

This article is protected by copyright. All rights reserved.

Author Manuscript

corresponding published values (Grierson et al., 1992; Volkova et al., 2015). These values of biomass and soil depth, combined with several anchoring points (i.e., assuming that zero soil depth holds zero biomass, regardless of aridity) were then plotted with aridity for each of the 10 sites in order to acquire coefficients for equation 19 for calculating B_{max}. Biomass values for each site were paired with measured Plant Area Index (PAI) (reported in Walsh et al., 2017) to calculate coefficients for equation 20 in calculating LAI_{lmax}.

3.4 Numerical implementations

The numerical model solves for soil depth (H), soil moisture (s), canopy water store (c_o) and biomass (structural and leaf pools: B_s and B_l) for a hypothetical point 50 m down from the ridgeline. A single simulation starts with a predefined soil depth and prescribed climatic forcing depending on rainfall regime and aspect (Table 2). When the simulations start, structural and leaf biomass are initialized by calculating their maximum values using prescribed edaphic and climatic conditions using equation 19.

Slope gradient of 0.52 at 50 m (S_{50}) was defined to roughly represent the steep hillslopes across the central highlands. S_{50} remain constant across all model simulations in order to obtain uniformity while varying only climatically driven eco-hydro-geomorphic processes. Results are discussed in context of this limitation. Mean slope from the three steepest sites (i.e., Eildon, Reefton and Frenchman's Spur (Table S5; Figure 2) was assumed to be representative of the steep hillslopes across the study area. S_{50} was then calculated by: (i) generating a combined gradient and distance-from-ridgetop curve from digital elevation model covering the three sites: and (ii) solving a third-order polynomial function fitted to the hillslope fraction of the data (i.e., the distance below the first slope-gradient inflection point) for distance value of 50 m (Text S8).Hillslope aspect, which is associated with variable incoming solar radiation and potential evapotranspiration (E_p), is defined as either north (equatorial) or south (polar) facing, to maximize the differences in climatic forcing for a given rainfall regime.

Model simulations alternate between daily and hourly timesteps for a pre-defined number of years (see flow chart in Figure S6). Evapotranspiration, biomass production and soil depth balance are calculated on a daily basis. On rainy days, however, processes that are driven by rainfall (such as: rainfall interception, infiltration, runoff and fluvial erosion) are modelled on an hourly basis for 24 hours. Using hourly rainfall allows the model to better represent inter-storm hourly variations in intensity which is critical for capturing post-fire geomorphic response. This means that some state variables (such as s, c_o and H) are updated both daily and hourly. Updates in state variables are computed using Euler's method for processes that operate both on a daily and hourly basis as detailed in Text S9.

Eight climatic scenarios that create a gradient of aridity were defined by a combination of four possible mean annual precipitation over two potential evapotranspiration (E_p) regimes for north and south facing aspects (Table 2). The eight climatic scenarios (Table 2) were used in simulations designated for model evaluation and for running numerical experiments. Single-site NSRP model was used to simulate hourly rainfall according to a prescribed rainfall regime before the start of each simulation. Four sites, representing rainfall gradient (ranging from MAP of ~721 mm yr^{-1} to ~1610 mm yr^{-1}; Figure 2), were chosen to calibrate the NSRP model simulator (Camici et al., 2011; Tarpanelli et al., 2012) and simulate hourly rainfall (refer to Text S1 in the supporting information for more details).

This article is protected by copyright. All rights reserved.

The model takes a simple approach for simulating E_p (Eqn. 5) typical for north and south facing hillslopes. Typical means for $E_{p-daily}$ and Δd at 50 m down the slope were calculated by averaging their values across the three steepest sites for either north- or south-facing aspects (i.e., Eildon, Reefton and Frenchman's Spur; Table S5; Figure 2). These calculations were made using monthly data for net radiation (R_{net}) and temperature (T_s) for each site from an available downscaled gridded resource which take into account slope and aspect, and include both direct and diffuse shortwave and net long wave radiation (Nyman et al., 2014b), and based on long term data from Australian Bureau of Meteorology (Australian Bureau of Meteorology, 2017). With this approach we assume that E_p does not vary significantly within each aspect as long as the hillslope gradient is similar (Table S5). Mean values used for $E_{p-daily}$ were 5.15 mm d^{-1} and 3.62 mm d^{-1}; and for Δd were 5.78 mm d^{-1} and 6.48 mm d^{-1} for north and south facing hillslopes, respectively.

Fire is treated in the model as a stochastic event that depends on annual soil moisture deficit as a proxy for flammability (Text S5). Once a year (arbitrarily chosen to be the 1st of January to be aligned with summer in the southern hemisphere), fire occurs whenever a random number (generated from a uniform distribution) is lower than the P_f. After fire, B_l (and LAI) resets to zero, exposing the soil to the direct rainfall impact; B_s is reduced by a pre-defined proportion (Eqn. 27); I_c reduces (Eqn. 26) and the surface soil becomes NC, all with a potential positive impact on fluvial erosion rates and soil depth. The model distinguishes between detachment-limited and transport-limited erosion (which is a particular post-fire case observed in SE Australia, and may not apply everywhere). We argue that post-fire sediment availability is limited both by time and quantity, which is better represented when these two types of erosion are separated.

3.5 Model evaluation

We framed the model evaluation in a stepwise manner, whereby components that are essential for the coevolution of soil depth and vegetation (i.e., ecohydrology, fire frequency distribution, surface processes) are evaluated independently. The model evaluation is performed by comparing model fluxes and state variables with published and unpublished data (Table S7 and S6).

3.5.1 Ecohydrology

Soil moisture

We examined whether CoolFlameS could reproduce observed trends in soil moisture under different climatic conditions by comparing the annual number of days that relative soil saturation (s) was above or below thresholds of plant water stress (s_i) and below threshold of flammability (s_{cut}) with similar metrics calculated for soil moisture measurements from six field sites (Table S5). For this step in the evaluation, model simulations were run for 1 kyr under different climatic scenarios (Table 2) with no fire and no change in soil depth.

Soil moisture measurements that were used for model evaluation (Table S6) were collected over one year (12/2015-12/2016) on north and south facing hillslopes in CH, RT and TT (Table S5; Figure 2). Depending on soil depth, between three to five soil moisture sensors (EC5; Decagon

This article is protected by copyright. All rights reserved.

Devices) were installed at different depths in soil pits at each site, from the soil surface to the bedrock-soil interface. Sensors were connected to a Campbell Scientific CR-1000 logger and each one was individually calibrated in the lab using soils packed at bulk densities corresponding to field measurements. Depth-integrated soil moisture at each site was calculated by integrating a linear function that was fitted to volumetric water content values at each sensor depth. Soils were assumed to be clay loam (as it is a typical soil across in the area (Rees, 1982)) and porosity value of 0.5 was used to calculate degree of saturation from both modelled and measured soil moisture.

Ecohydrological partitioning

Ecohydrological partitioning was evaluated by comparing the modelled outputs with published values from three local studies. Note that the locations of these studies (Figure 2) were different than our data collection sites that were used for grounding the model to local systems (Figure 2). The evaluation of the ecohydrological partitioning was done by using climate scenarios (i.e., rainfall/aspect combinations; Table 2) that are similar to those in the published studies in order to obtain matching model simulations. Average values for ET components (interception loss, transpiration and soil evaporation) were calculated from 1 kyr-long model simulations under each climatic scenario, with fire turned "off" to avoid disturbance effects that are not representative of the field measurements of ET that are used in the evaluation. Results from simulations under "south-facing wet" climate (i.e., aridity 0.82; Table 2) were compared with data from Vertessy et al.(2001), which represents Eucalyptus regnans with a typical average MAP of 1800 mm yr^{-1}. Results from simulations under "north-facing wet" climatic scenario (i.e., aridity 1.17; Table 2) were compared with Nolan et al. (2014), representing wet-mixed species forest on a north-west facing hillslope with MAP of ~1550 mm yr^{-1} . Results from simulations under "north-facing damp" (i.e., aridity 1.49; Table 2) climatic scenario were compared with data reported in Mitchell et al. (2012), representing a north-east facing hillslope with ~1200 mm yr^{-1} (averaged over 4 years), which is dominated by a mixed species sclerophyll forest.

3.5.2 Fire frequency

The fire model was evaluated by comparing distribution of modelled fire frequency under different climatic and edaphic conditions with what is known and described in relevant literature. Modelled fire frequency was calculated using outputs from a set of 100 kyr simulations driven by wet, dry and damp climatic scenarios (aridity of 0.83, 1.05 and 1.49, respectively; Table 2) under steady state soil depth conditions for each.

3.5.3 Surface processes

Surface runoff and peak discharge

We compared modelled surface runoff ratio (SRR) with independent measurements by Van der Sant et al. (2018), who quantified SRR using 8 m plots on five sites across an aridity gradient (Figure 2). Modelled SRR were calculated for 8 difference climate scenarios (Table 2) over 10 kyr simulations, while only SRR for the first-year post-fire were averaged. Surface runoff in the model is being produced on an hourly basis. In this analysis simulated surface runoff generated from all rainstorms below 5 mm h^{-1} were excluded because experimental error in the field measurement can be relatively large for these small rainfall events.

This article is protected by copyright. All rights reserved.

Modelled peak discharge was compared to measured values in order to evaluate the model's ability to simulate high-magnitude surface runoff events. Measured discharge data was obtained from a study that monitored two small (0.29 ha) and relatively dry (mean aridity of 2.2) north and south facing headwater catchments at Stoney Gully Catchment, Victoria (SE Australia), starting approximately six months after it was severely burnt on February 2009 (Noske et al., 2016)(Figure 2). A detailed description of the experimental setting is described in Noske et al. (2016). Modelled values were calculated using Q_{15} (Eqn. S5) from all first years after each fire after running the model driven by a dry climatic scenario (aridity 2.61 Table 2).

Erosion and denudation

Modelled erosion rates were compared to erosion measurements from local studies (Cawson et al., 2013; Lane et al., 2006; Noske et al., 2016; Smith et al., 2011a). Modelled mean sediment yield was obtained by calculating cumulative erosion rates from 100 kyr simulations for each of the climatic scenarios described in Table 2. Denudation rates (mm kyr^{-1}) were calculated using cumulative erosion rates (both from fluvial and diffusive processes) across the length of each simulation. From the total of 100 kyr of each simulation, modelled post fire sediment yield was calculated from the first years after each fire, while background (unburnt) values were calculated from the rest (i.e., from all the years excluding the first year after fire).

3.6 Numerical experiments

Numerical experiments were developed to;

i) test the hypothesis that in SE Australia, fire-related processes are critical to explain the variations in coevolved soil-forest system states across an aridity gradient,

ii) identify the key fire-related processes that are important for coevolution

iii)identify any important fire-related feedbacks involved in the coevolution of soil-vegetation systems.

One of the caveats in testing soil development models is that it is often uncertain whether the observed soil had reached a steady state depth (Phillips, 2010). A steady-state in this respect means that long-term erosion rates equals long-term soil production which results in minimal long-term change in its depth ($dH/dt = 0$). Output variables that were used for testing the hypothesis, for testing model sensitivity to the effects of fire and for evaluating feedbacks in the coevolution process were soil depth and projected vegetation cover at steady-state soil depth (H_{ss} and V_{c-ss}, respectively). Even though we compare these output variables with observations, we do not make any assumptions that the systems we compare them with had reached steady-state. We can, however, use the model to assess whether current systems are likely to have reached steady state by comparing them to the output variables. Preliminary analysis showed that soil in simulations driven by the wettest climatic conditions took ~150 kyr to reach steady state depth (compared to ~30 kyr when driven by the direst climate) starting with 0.5m deep soil.

3.6.1 Testing the hypothesis

The hypothesis was tested by comparing the ability of simulations with and without fire to predict observed, contemporary system states. In experiment 1, model simulations were allowed to run with ($+Fire$) and without ($-Fire$) fire for the duration of 200 kyr in order to ensure that steady-state in the output variables had been reached. For each treatment, a set of eight

This article is protected by copyright. All rights reserved.

Author Manuscript

simulations were conducted with an initial soil depth of 0.5 m using the climatic scenarios detailed in Table 2. After each simulation, H_{ss} and V_{c-ss} were calculated by the mean of the last 10 kyr. To test the hypothesis, modelled H_{ss} values were compared with soil depth measurements across an aridity gradient, taken from Inbar et al. (2018). In addition, the modelled V_{c-ss} values were compared with gridded remotely sensed woody vegetation cover from TERN Auscover (2017). Woody vegetation cover data was extracted for 5 km square polygons near the three steepest sites (Eildon, Reefton and Frenchmen's Spur; Table S5). TERN woody vegetation cover was retrieved using long-term LANDSAT data at 30 m resolution (Gill et al., 2017). To stay constrained to the upper part of hillslopes (whereby soil depth and water availability are assumed to limit productivity) remotely sensed woody vegetation cover was extracted from grid cells that have contributing area lower than 0.1 ha. Model skill was evaluated by comparing root mean square error (RMSE) for H_{ss} and V_{c-ss} from $+Fire$ and $-Fire$ with observations (Table S8).

3.6.2 Identifying key fire-related processes that are important for coevolution

CoolFlameS incorporates two well studied mechanisms by which fire affect soil erosion: the effect of fire on soil surface properties (which incorporates both changes in infiltration capacity and soil cohesiveness) and vegetation cover. In experiment 2, each simulation was designed to run with fire, but with one of its effects turned "off". Simulations were:

(i) $-\Delta I_c$: Simulations with fire ($+$Fire) excluding post-fire reduction in infiltration capacity.

(ii) $-\Delta CO$: Simulations with fire ($+$Fire) excluding post-fire change in soil surface cohesiveness.

(iii) $-\Delta LAI$: Simulations with fire ($+$Fire) excluding the effect of fire on forest cover (LAI not initialized after every fire).

Similar to experiment 1, eight simulations were conducted using the climatic scenarios detailed in Table 2, each starting with 0.5 m deep soil. The relative role of the effect of fire on I_c, soil cohesiveness and forest cover was evaluated by ranking RMSE values calculated by comparing the output variables from $-\Delta I_c$, $-\Delta CO$ and $-\Delta LAI$ to those from $-fire$ and $+fire$ (Table S9). Results are interpreted as such: the lower (higher) the RMSE of one of the treatments when compared to $-fire$ the higher (lower) its relative role in the effect of fire on coevolution.

3.6.3 Identifying fire-related feedbacks in coevolution

Simulations with abrupt changes in rainfall were conducted in order to explore the interactions and feedbacks throughout the evolution of a hypothetical soil-forest system. Temporal changes in soil depth (H) and projected vegetation cover (V_c) were explored by running simulations under "dry" (MAP of 720 mm yr^{-1}) north facing hillslope with 0.2 m deep soil, which was interrupted by a 150 kyr long wet period (which was achieved by increasing rainfall to MAP 1610 mm yr^{-1}). To single out the effect of fire on coevolution, results from simulations with fire were compared to those from simulations without. We note that this experiment is not intended to simulate real climatic fluctuations and that its purpose is for analysis of feedbacks in the coevolution process. The extreme changes in rainfall were chosen in order to maximize the impact of climate on coevolution, whilst observing how soil depth, biomass and fire regime coevolve from one steady-state to another.

Author Manuscript

This article is protected by copyright. All rights reserved.

4 Results

4.1 Model evaluation results

4.1.1 Ecohydrology, flammability and fire frequency

Results show that, overall, CoolFlameS reproduces the observed trends in all threshold metrics with respect to aridity and MAP and gives reasonably good predictions of hydrological partitioning when compared to published data (Figure 4). The trend in modelled water stress, expressed as the proportion of days above and below incipient stomatal closure (s_i; Figure 3a-3d), correspond well with the inverse correlation between primary productivity, biomass and canopy cover with aridity that is observed across SE Australian temperate forests (Givnish et al., 2014; Inbar et al., 2018; Keith et al., 2010).

Mean fire return interval (FRI) from the 100 kyr-long simulations were 18.3, 32.6 and 87.3 years for the "dry" (aridity 1.49), "damp" (aridity 1.05) and "wet" (aridity 0.83) climate scenarios, respectively (Figure 5a), which is in line with the systematic increase in the number of days above the flammability threshold at higher aridity scenarios (Figure 3e). Mean number of days in which soil moisture (s) was equal or lower than the flammability threshold (s_{cut}) were 139, 71 and 24 days for simulations under the "dry", "damp" and "wet" climatic scenarios. Similar trend with respect to the flammability of leaf litter across similar forest types has been identified in local field studies (Nyman et al., 2015, 2018).

FRI distributions from the three simulations as a function of forest age (Figure 5a-5c) resembles the "Olson" model (Olson, 1963) proposed by McCarthy et al. (2001) which describes situations by which flammability increases with forest age up to an asymptote and is typical to some Eucalyptus forests (Walker, 1981). This was verified by the plotting number of days that the modelled system was below flammability threshold (as a proxy for flammability) as a function of forest age (Figure 5d), which indeed points to such flammability behavior. The slightly higher flammability in the first two years under dry climate (Figure 5d) can be explained by the very low infiltration capacity under this climatic forcings (Table S6). This indicates that the low infiltration capacity during the first couple of years after a fire has an ecohydrological consequence, slowing vegetation recovery by reducing plant available water.

Several studies have shown that flammability can decrease immediately after a fire due to lack of available fuels (eg., Hurteau et al., 2019; Parks et al., 2016). According to the way that the fire model was calibrated (Text S5), flammability should not have changed with time since fire, as it was not restricted by fuel availability. The fact that flammability in the model depends on the number of days that $s \leq s_{cut}$ causes fire probability to be lower in the first years during vegetation recovery (Figure 5d). This emergent self-limiting behavior suggestes that it might be unnecessary to explicitly account for availability and moisture of burnable fuel within a coevolutionary framework.

4.1.2 Surface runoff and geomorphic processes

CoolFlameS reproduces the observed trend in surface runoff ratio (SRR) with aridity (Figure 6a) and of peak discharge as a function of rainfall depth (Figure 6b). The increasing trend in runoff ratio with aridity that emerge from model simulations (Figure 6a), are consistent with published literature (Lane et al., 2006; Noske et al., 2016; Sheridan et al., 2015; Van der Sant et al., 2018), and stem from the inverse correlation between infiltration capacity and aridity (Eqn. 27). We also

This article is protected by copyright. All rights reserved.

note that the results in Figure 6 should be interpreted in context of differences in spatial scale and hillslope gradient between model and field measurements.

Published and modelled erosion rates for burnt (first year post-fire) and unburnt conditions are summarized in Table 3 and 4, respectively. The increasing trend in runoff ratio and peak discharge (Figure 6) is translated to a similar trend in post-fire erosion rates (Table 4). Combined with higher fire frequency, these results point to rates of long-term erosion that increase with increasing aridity, similar to what had been hypothesized (Inbar et al., 2018) and observed (Table 3) in SE Australia. Published post-fire sediment yields increase with decreasing rainfall (Table 3), with 1-3 order of magnitude difference compared with unburnt state with highest difference in mid-rainfall range (Cawson et al., 2013). Similarly, the difference in modelled erosion rates between burnt and unburnt states are 1-3 orders of magnitude, with 2-3 orders of magnitude between aridity 1.05-1.49 (Table 4). Modelled post-fire erosion rates from simulations under the driest climatic conditions (aridity 2.61) is 8.51 t ha^{-1} yr^{-1}, which is similar to what had been measured by Noske et al. (2016)(Table 3).

Modelled denudation rates from the 8 different climatic scenarios were between 13.8-83.4 mm kyr^{-1} (Table 4), which is within a similar range compared to published values. For example, Bishop (1985) suggested denudation rates in south eastern Australia during the last 15-20 Myr to be 10 mm kyr^{-1}. The author ascribed the low denudation rates to forest cover and the continent's tectonic stability. Heimsath et al. (2009) estimated denudation rate from a basin at a retreating escarpment in Northern Territory to be 10-40 mm kyr^{-1}, while Smith et al. (2012) estimated these rates to be 27 mm kyr^{-1} from a first order catchment in Victoria, SE Australia. In a recent study, Hancock et al. (2017) summarized a long term monitoring experiment of several steep catchments in New South Wales. The authors estimated denudation rates from two undisturbed forested catchments to be around 70 mm kyr^{-1}. The steepness of the catchments (mean slope of ~22 degrees) was suggested as a plausible reason for the relatively high denudation values compared to background values in the literature (such as in Fifield et al. (2010) and Bishop (1985)). The differences in scale and slope of the modelled unit could potentially explain the overprediction of denudation rate at the dry end of the aridity gradient (Table 4).

Model results indicate that hillslope aspect has a very significant effect on erosion and denudation rates (Table 4). In all model simulations, north (equatorial) facing aspect yielded more erosion than its south (polar) facing counterpart. Such differences are caused solely by different insolation which had been shown to cause hillslope asymmetry over geological timescales (e.g., Istanbulluoglu et al., 2008; McGuire et al., 2014; Pelletier et al., 2018; Yetemen et al., 2015). Differences in erosion rates between equatorial and polar facing hillslopes during the first year after the fire seems to decrease with aridity, but peak in aridity 1.05-1.49 in an unburnt state. Difference in denudation rates (which also includes the effect of fire frequency) between the aspects, however, peak between aridity 1.05-2 (Table 4). Over longer timescales, these results are in line with what have been reported by Inbar et al., (2018), who found a peak in hillslope asymmetry at similar aridity values.

Overall, soil moisture, ecohydrological partitioning, distributions of fire return interval, surface runoff ratio, peak discharge, erosion and denudation rates are predicted reasonably well across the climate scenario compared to observations and published data. This provides a satisfactory outcome of model performance despite its relative simplicity and the different environmental conditions (i.e., slope, fire severity, soil type etc.) and scale (i.e., plot-catchment) that the model outputs were compared with.

This article is protected by copyright. All rights reserved.

Author Manuscript

4.2 Testing the hypothesis

Modelled soil depth (H_{ss}) and projected vegetation cover (V_{c-ss}) with respect to aridity were compared to logistic functions that best fitted to measured values (Figure 7). H_{ss} and V_{c-ss} predicted by model simulations with fire ($+fire$) replicate the observed trends and mostly sit within the 95% confidence interval calculated using observed values (Figure 7a and 7b). Simulations without fire ($-fire$) predict a similar trend in H_{ss} and V_{c-ss}, however they overestimate both state variables with increasing aridity when compared to observations and to model simulations with fire. Overall, model simulations with fire performed better in predicting H_{ss} and V_{c-ss} (RMSE 0.27 m and 0.06, respectively) when compared to simulations without fire (RMSE 0.79 m and 0.47, respectively).

4.2.1 Identifying key fire-related processes that are important for coevolution

The results are used to evaluate the relative contribution to coevolution of several potentially important fire-related processes. When comparing all treatments to published and observed data, model simulations with fire (+fire) performed better in predicting the soil depth and forest cover when compared to the simulations where one of the fire-related processes was turned "off" (Table S8). Results show that the variability in the output variables from simulations when one of the fire-related processes was turned "off" increases with aridity (Figure 7c-h). RMSE values that compare these simulations with $-\mathrm{fire}$ and $+\mathrm{fire}$ are presented in Table S9. Compared to $-\Delta\mathrm{LAI}$, and $-\Delta\mathrm{CO}$, both state variables predicted by $-\Delta\mathrm{I_c}$ showed the closest resemblance to those predicted by $-\mathrm{fire}$. In contrast, compared to $-\Delta\mathrm{I_c}$ and $-\Delta\mathrm{CO}$, soil depths predicted by $-\Delta\mathrm{LAI}$ showed the highest resemblance to those predicted by $+\mathrm{fire}$. The effect of $-\Delta\mathrm{LAI}$ seemed to have lower impact on $\mathrm{H_{ss}}$ compared to $\mathrm{V_{c-ss}}$.

4.2.2 Identifying fire-related feedbacks in coevolution

The results reveal some important fire-related feedbacks in the coevolution of soils and forests. The temporal evolution of soil depth (H), projected vegetation cover (V_c) and fire return interval (FRI) for simulations with and without fire are presented in Figure 8a-8c. Figure 8d illustrates the coevolution of soil depth, vegetation cover and fire frequency within a 2D space. In this figure, each marker represents the mean value of H and V_c within a 1 kyr-long bin. Bin size and color represent the FRI. Simulations start with a dry climate. For simulations with fire, the arrival of the wet phase after 10 kyr result in a steep increase in V_c within a 1 kyr period with only a small increase in H (Figure 7d). It takes about 50 kyr for V_c to reach steady-state and >120 kyr for H (Figure 8a-8b). FRI increase dramatically immediately after the climate changes and continues increase more gradually throughout the wet phase. A rapid decline in FRI towards its "background" state occurs as the climate switches back to a dry phase after 150 kyr, followed by a decline in H and V_c, which end up with stead steady-state values similar to their initial conditions (Figure 8a-8b).

A similar type of response to climatic changes is observed for simulations without fire (dashed green line in Figure 8a and 8b). However, both state variables increase immediately during the first dry period, probably towards their steady state values for dry climate without fire (Figure 7a and 7b). Similar to simulations with fire, the arrival of the wet phase at 10 kyr mark causes a sharp increase in V_c with only a gradual increase in H (Figure 8d). By the end of the wet phase, H and V_c had already reached higher values compared to simulations with fire. The decline in H

Author Manuscript

This article is protected by copyright. All rights reserved.

and V_c in simulations with fire is more gradual during the wet-to-dry transition than during the initial dry-to-wet transition (Figure 8a-8b).

During the coevolution without fire, both H and V_c values are consistently higher than their values from simulations with fire (Figure 8a and 8b). Overall, adjustment time in V_c as a response to climate change seems to be faster than the adjustments in H. Time to steady-state soil depth from dry-to-wet transition takes longer compared to the time it takes in the wet-to-dry transition. This behavior is less clear for the evolution of V_c.

The coevolution of V_c, H shows a hysteresis pattern as a response to changes in rainfall both for simulations with and without the effect of fire (Figure 8d). However, there is a difference in the pattern between the two simulations. FRI increases as soil becomes deeper and vegetation becomes denser and seems to peak around end of the wet period. A similar decline in V_c occurs at the same time for simulation without fire. The increase in density of the 1 kyr-long bins indicates that both H and V_c had reached their steady-state values by the end of the wet period (~120-160 kyr) and the second dry period (~190-200 kyr).

5 Discussion

5.1 Experiment 1 - the role of fire in coevolution (Evaluating the hypothesis)

Our initial hypothesis that fire-related processes are critical to explain the variations in coevolved soil-forest system states across an aridity gradient is supported by the results (Fig 7a and 7b) showing that simulation with fire are more consistent with contemporary observation that simulations without fire. Model results show that the relative role of fire increase with aridity (Figure 7a and 7b). This can be explained by the more frequent fires and higher erosion rates (Table 4) as aridity increases. As aridity increases beyond aridity 1, so does the relative contribution of fluvial erosion rates. This effect is further amplified by fire, as seen in Figure S8.

The fact that the predicted projected canopy cover (V_{c-ss}) trends in a similar manner as soil depth (H_{ss}) with respect to aridity can be explained by the change in biomass holding capacity of the soil, caused by the interaction between climate, fire and the balance between soil production and erosion on soil depth (Hahm et al., 2019). The phenomenon that erosion controls vegetation patterns was observed by Milodowski et al. (2015) in the Northern-Californian Sierra Nevada, USA, where mean basin slope, a proxy of long term erosion rate, explained 32% of variance in above ground biomass, outweighing the effect of other factors, such as mean annual precipitation, temperature and lithology. The authors ascribed this effect to the reduction in water holding capacity due to the limitation dictated by thinner saprolite.

5.2 Experiment 2 - The role of fire-related processes in coevolution

Results indicates that among the three possible effects of fire that were explored, the role of post-fire reduction in I_c on H_{ss} and V_{c-ss} was the largest (Figures 7c-7d and S7b-S7c). Post-fire reduction in I_c can explain the increasing dominance of fluvial processes at aridity values >1 (as seen in Figure S8), which result in shallower soils from simulations with fire beyond that point (Figure 7a and 7b). For aridity values <1, post-fire reduction in I_c is not sufficiently large to affect surface runoff. Consequently, on slopes supporting wet forest types, the relative role of diffusive processes is higher compared to fluvial processes (Figure S8).

Author Manuscript

This article is protected by copyright. All rights reserved.

Post-fire erosion is often associated with loss of cover, increased hydrophobicity and reduction in root cohesion (Istanbulluoglu & Bras, 2005). The latter process was not implemented explicitly in CoolFlameS but is implicit within the surface cohesiveness term. Our results indicate that long-term erosion is more sensitive to reduction in I_c (and consequential increase in surface runoff) than to the amount of sediment that is available to be transported ($-\Delta CO$; Figures 7e-7h and S8b-S8c). This can be explained by the interplay between the transport limited nature of the NC material and the time it is available for transport (Nyman et al., 2013).

The relative role of post-fire reduction in forest cover ($-\Delta LAI$) was found to be lower than the two other processes examined (Figures 7 and S8b-S8c). This result can be explained by the effect of the interaction between forest cover and infiltration capacity on fluvial erosion across the aridity gradient. At higher aridity values, background forest cover is always relatively low (Figure 7b), and the effect of the short-lived post-fire removal of vegetation cover on fluvial erosion is insignificant compared to the reduction in infiltration capacity during the same period. In wetter climates, vegetation density is higher and the effect of the temporary loss of cover on fluvial erosion rates can be significant. However, this effect is balanced by the high infiltration capacity, which keeps surface runoff rates low even after fire (Noske et al., 2016). These results indirectly suggest that the time to forest canopy recovery that explicitly depend on forest recovery trait has little impact on long-term coevolution of soil depth and vegetation in southeastern Australia.

In a study aggregating hundreds of post fire infiltration and runoff measurements, Sheridan et al (2015) found that post-fire runoff generation was highly correlated with aridity, such that more arid hillslopes, that often have younger and less developed soils, were associated with higher post fire sediment yields. Our results indicate that the trend of H_{ss} with aridity (Figure 7a) is determined mainly by the amount of surface runoff that is generated (which is controlled by the infiltration capacity) and how it affects post-fire fluvial erosion rates (Figure S8). Our model suggests that in a world without fire, the differences in soil depth and vegetation cover between dry and wet systems would have been significantly smaller to what is currently observed (Figure 7a and 7b). Other theoretical experiments had shown a significant increase in forest cover on the expense of grasslands in a world without fire (Bond et al., 2005). Our results highlights the possible role of fire-related changes in soil depth on global distribution of vegetation.

5.3 Experiment 3 - The role of interactions and feedbacks in coevolution

Modelled interactions and feedbacks between climate, soil depth, vegetation and fire in the coevolution process (experiment 3) can be deciphered from Figure 8. Simulation with fire start when the system is under a dry phase and the shallow soil and low forest cover are in steady-state with the dry climate and frequent fires (Figure 8a and b). The increase in rainfall after 10 kyr has three consequences. First, after climate becomes wetter, soils are now able to support more vegetation for a given depth, resulting in higher V_c which in turn reduces the amount of rainfall reaching the soil surface. Second, as climate becomes wetter, soil moisture increases, pushing fires to be further apart (Figure 8c). Third, the transition to wetter climate results in higher infiltration capacity allowing more throughfall to infiltrate, preventing surface runoff (Figure 6a) and fluvial erosion (Table 4). This, in turn, causes a buildup of soil depth, as the soil is produced faster than it is eroded, which feeds back to the its ability to hold more moisture and more vegetation.

Author Manuscript

This article is protected by copyright. All rights reserved.

Unlike the simulation with fire, soil depth and vegetation are not in steady state when the simulation without fire starts (Figure 8a and 8b). The lack of fire and the lower erosion rates causes the soil profile to build up and forest cover to increase as a consequence. When rainfall increases, H and V_c values start to increase from higher values compared to simulations with fire. The deeper soils in simulation without fire is the result of infiltration capacity being higher for longer proportion of time. This causes soil to be produced even faster than it is eroded, which also translates to slightly higher vegetation carrying capacity.

The differences in the response of the system to changes in climate between simulations with and without fire is exaggerated when the climate becomes drier after 150 kyr (Figure 8a-8c). After the climate changes, soils can no longer support the same amount of vegetation, which results in an opening of the canopy (Figure 8b). In simulations with fire, the dry climate results in drier soils, higher flammability (Figure 3f) and more frequent fires (Figure 8c). The increase in fire frequency, in turn, results in the canopy being open for a longer period of time, which coincides with the reduction in infiltration capacity and in soil cohesiveness and result in increased surface runoff (Figure 6a) and higher fluvial erosion rates (Table 4). Without fire, however, canopy cover and infiltration capacity stay higher for longer, resulting in lower surface runoff and fluvial erosion compared to simulation with fire. In both cases, the rate of soil produced is lower than the rates in which it is eroded, resulting in a decrease in soil depth. The differences in of erosion rates with and without fire (Table 4) after the wet-to-dry transition result in a completely different system for the same climate, where soil depth is almost three times as deep and vegetation cover two times as high in the absence of fire (Figure 8a and 8b). These simulations present an alternative reality to the state that these temperate systems might have been in the absence of fire.

Our results show that the response time of V_c to changes in climate is generally faster than that of H and takes between thousands of years (without fire) to tens of thousands of years (with fire) between two alternative equilibrium states. On a similar note, Blonder et al. (2018) found that the prediction of contemporary distribution of vegetation can be improved by taking into account paleoclimate as well as contemporary climate predictors. The longer adjustment time of soils had been reported in the literature (eg., Cohen et al., 2013; Temme & Veldkamp, 2009). For example, Cohen et al. (2013) used a numerical model to study the soil-landscape response to Quaternary climate fluctuations. The authors found that it takes tens of thousands of years for soils to adjust to fluctuations in climate.

There is evidence from SE Australia that climatically driven change in fire activity can push systems towards different states (eg., Bowman, 2000; Fletcher et al., 2014a; b). Using a multi-proxy paleo-ecological analysis from Tasmania, Fletcher et al. (2014a) showed that an increase in fire activity over the past 6,500 yr resulted in the transition between a fire-intolerant rainforest to a drier fire-tolerant Eucalyptus forest, which also coincided with evidence of elevated erosion and nutrient loss. CoolFlameS does not model change between different forest types. However, our results align with the findings of Fletcher et al. (2014a) as they show that the transition between states as a response to climate change are intensified with the presence of fire. This can be seen by the bigger drop in forest cover after the wet-to-dry transition (Figure 8b).

Two separate hysteresis behavior-patterns can be identified from Figure 8d. The two hysteresis are related to the different V_c and FRI values for a given climatic forcing (wetting and then drying) and soil depth and can be explained by the effect of the interaction between climate and soil water holding capacity on productivity and flammability. At the start of the wet period, V_c

This article is protected by copyright. All rights reserved.

and FRI increase gradually with soil depth despite the abrupt change to a wetter climate. Under these circumstances, productivity and flammability are limited only by soil water holding capacity. V_c and FRI decrease abruptly as rainfall declines by the end of the wet period and stay constantly low even when the soil is still deep. Under these conditions, productivity and flammability are mainly driven by the supply of water and not by that water holding capacity of the soil. These results indicate that under wet climatic conditions, soil depth can potentially control fire frequency. As far as the authors are aware, this relationship had never been identified before, and certainly requires to be tested empirically.

Results from experiment 3 point to a climatically driven eco-hydro-geomorphic feedback between soil moisture, fire and fluvial erosion that drive the trajectory, rate and magnitude of change in the coevolution of soil-vegetation systems. In this feedback (Figure 9), climate drives long-term fire frequency and fluvial erosion rates that affect soil depth. This, in turn, changes the water holding capacity of the soil, which feeds back to productivity and fire frequency. For example, under a drying climate, higher fluvial erosion rates and higher fire frequency might lead to more erosion and more fire. In contrast, under a wetting climate, lower erosion rates due to lower fire frequency might lead to lower erosion and less frequent fire. This fire related eco-hydro-geomorphic feedback eventually stops when there is no soil left or when climate, vegetation, soil and fire regime reach a new equilibrium state.

5.4 Limitations, implications and opportunities

The results indicate that the coevolution of soil depth and vegetation is highly dependent on the properties of the soil surface. In nature, long-term weathering of bedrock, gravel and soil particles, driven by climate (Riebe et al., 2004) and vegetation (Brantley et al., 2017), make changes in soil properties that control plant available water capacity and its permeability (Clapp & Hornberger, 1978; Saxton & Rawls, 2006). The development of soil properties in CoolFlameS is modelled implicitly as a function of aridity, however, a more explicit representation is suggested for further model development. We propose that effect of changes in soil properties on coevolution of soils-vegetation systems is nonlinear and can increase the difference in system states even further. In this proposed climatically-driven soil development-vegetation-fire feedback higher water holding capacity of a soil for a given soil depth increases its biomass holding capacity, which can indirectly decrease flammability and fire frequency. Future efforts in this direction are encouraged to include soil development, to represent the climate-controlled development of soil hydraulic properties and particle size distribution (Cohen et al., 2009; Temme & Vanwalleghem, 2016).

Over geological timescales, the rate of soil production and erosion dictates the rate of change in hillslope gradient, which in turn affect the insolation regime and water balance at any point on the landscape in a self-regulating feedback (Yetemen et al., 2015). By excluding possible changes in hillslope gradient in the zero spatial dimension approach - simplicity was achieved at the expense of including a factor that may explain variations in soil depths and vegetation cover across the landscape (Inbar et al., 2018). For example, the decrease in hillslope gradient with aridity in SE Australia (Inbar et al., 2018) can potentially explain why modelled soil depth was underestimated between aridity 1 to 1.5 (Figure 7a). We argue that the large difference in erosion and denudation between the wettest and driest simulations (Table 4) would have been smaller had hillslope gradient been allowed to change. In this case, long-term fluvial erosion would flatten hillslopes in drier climatic conditions, similar to the what had been observed by Inbar el

Author Manuscript

This article is protected by copyright. All rights reserved.

al. (2018). Another potential avenue of research could be to expand this modelling framework into a 3D landscape evolution space, which will allow investigating the feedbacks and interactions within the coevolution of fire, vegetation, soils and landscapes more generally (Pelletier et al., 2013).

The modelling approach implemented in CoolFlameS implies that rates and trajectory of change of soil-vegetation systems are caused by a climatically-driven eco-hydro-geomorphic feedback between soils, vegetation and fire. By including contemporary eco-hydro-geomorphic processes our results support the conceptual model proposed by Inbar et al. (2018), where they attributed observed trends in the soil depth with aridity (Figure 7a) to climatically-driven variations in productivity, fire and soil hydraulic properties. The threshold in soil depth across the water-energy limited boundary (where aridity$\approx$ 1) found in both observed and modelled domains highlight the effect of climate and fire in driving rates of coevolution.

Our results indicate that including fire-related processes and feedbacks is essential if one intends to study critical zone and landscape evolution in fire prone landscapes. Our results further indicate that in these systems, fire can be regarded to be a central part of the coevolution process, hence should be modelled dynamically depending on climate and the state of the system. In Southeastern Australia, fire-related processes and feedbacks are found to drive the coevolution of soil-forest systems and are responsible for the magnitude of differences in soil depth and vegetation cover across contemporary climatic gradient.

Author Manuscript

This article is protected by copyright. All rights reserved.

6 Conclusions

We used the flammable landscapes of SE Australia to evaluate the role of fire in the coevolution of soil-forest systems. Using a new numerical model (CoolFlameS) that represents the eco-hydro-geomorphic processes that are typical to SE Australian forests, we: (i) tested the hypothesis that fire-related processes are critical to explain the variations in coevolved systems states across an aridity gradient; (ii) identified the dominant fire related processes involved in coevolution; and (iii) identified any fire related feedbacks involved. CoolFlameS showed good skill in predicting patterns of soil moisture thresholds, ecohydrological partitioning, fire frequency distribution, surface runoff and erosion and denudation rates across a gradient of aridity when compared to local measurements and published data. The validated model was then used to conduct numerical experiments to address the three aims. The results showed that:(i) the hypothesis was supported, and that the relative role of fire in coevolution of soil depth and forests increased with aridity in the study area; (ii) amongst the three effects of fire examined, the relative role of post-fire reduction in infiltration capacity (and its effects of surface runoff and fluvial erosion rates) on coevolution of soil-vegetation systems was the largest, followed by post-fire reduction in soil cohesiveness and in canopy cover. (iii) the trajectory and magnitude of the coevolution of soil-vegetation systems is driven by a climatically driven feedback between soil, vegetation and fire. For example, under a drying climate, long-term increase in post-fire erosion might contribute to more frequent fires and more erosion. We conclude that incorporating fire-related processes and feedbacks is essential when using models to investigate the critical zone and landscape evolution in fire-prone landscapes.

Acknowledgements

This research was funded by the Victorian Department of Environment, Land, Water and Planning (TA37948), Melbourne Water Corporation (TA37690), and the Australian Research Council (LP150100654). The Woody Vegetation Cover data were obtained through TERN AusCover (http://www.auscover.org.au). TERN is Australia's land-based ecosystem observatory delivering data streams to enable environmental research and management (TERN, http://www.tern.org.au). TERN is a part of Australia's National Collaborative Research Infrastructure Strategy (NCRIS, https://www.education.gov.au/national-collaborative-research-infrastructure-strategy-ncris).

References

Amundson, R., Heimsath, A. M., Owen, J., Yoo, K., & Dietrich, W. E. (2015). Hillslope soils and vegetation. *Geomorphology*, *234*, 122–132. https://doi.org/https://doi.org/10.1016/j.geomorph.2014.12.031

Australian Bureau of Meteorology. (2017). Gridded climate data.

Barrows, T. T., Stone, J. O., Fifield, L. K., & Cresswell, R. G. (2001). Late pleistocene glaciation of the kosciouszko massif, snowy mountains, Australia. *Quaternary Research*, *55*(2), 179–189. https://doi.org/10.1006/qres.2001.2216

Benda, L., & Dunne, T. (1997). Stochastic forcing of sediment routing and storage in channel networks. *Water Resources Research*, *33*(12), 2865–2880. https://doi.org/10.1029/97WR02387

Berry, S. L., Farquhar, G. D., & Roderick, M. L. (2005). Co- Evolution of Climate, Soil and

This article is protected by copyright. All rights reserved.

Author Manuscript

Vegetation. In M. G. Anderson (Ed.), *Encyclopedia of hydrological sciences*. Indianapolis: John Wiley And Sons, Ltd.

Bishop, P. (1985). Southeast Australian late Mesozoic and Cenozoic denudation rates: a test for late Tertiary increases in continental denudation. *Geology*, *13*(7), 479–482. https://doi.org/https://doi.org/10.1130/0091-7613(1985)13<479:SALMAC>2.0.CO;2

Blonder, B., Enquist, B. J., Graae, B. J., Kattge, J., Maitner, B. S., Morueta-Holme, N., et al. (2018). Late Quaternary climate legacies in contemporary plant functional composition. *Global Change Biology*, *24*(10), 4827–4840. https://doi.org/10.1111/gcb.14375

Bond, W. J., Woodward, F. I., & Midgley, G. F. (2005). The global distribution of ecosystems in a world without fire. *New Phytologist*, *165*(2), 525–538. https://doi.org/10.1111/j.1469-8137.2004.01252.x

Bowman, D. M. J. S. (2000). *Australian rainforests: Islands of green in a land of fire*. (D. M. J. S. Bowman, Ed.), *New Zealand Geographer*. Cambridge, United Kingdom: Cambridge University Press. https://doi.org/10.1111/j.1745-7939.2001.tb01610.x

Bradstock, R. A. (2010). A biogeographic model of fire regimes in Australia: current and future implications. *Global Ecology and Biogeography*, *19*(2), 145–158. https://doi.org/10.1111/j.1466-8238.2009.00512.x

Brantley, S. L., Eissenstat, D. M., Marshall, J. A., Godsey, S. E., Balogh-Brunstad, Z., Karwan, D. L., et al. (2017). Reviews and syntheses: On the roles trees play in building and plumbing the critical zone. *Biogeosciences*, *14*(22), 5115–5142. https://doi.org/10.5194/bg-14-5115-2017

Brutsaert, W. (1982). Evaporation into the atmosphere. Theory, history, and applications. *Evaporation into the Atmosphere. Theory, History, and Applications.* https://doi.org/10.1029/eo063i051p01223-04

Camici, S., Tarpanelli, A., Brocca, L., Melone, F., & Moramarco, T. (2011). Design soil moisture estimation by comparing continuous and storm-based rainfall-runoff modeling. *Water Resources Research*, *47*(5). https://doi.org/10.1029/2010WR009298

Cannon, S. H., Bigio, E. R., & Mine, E. (2001). A process for fire-related debris flow initiation, Cerro Grande fire, New Mexico. *Hydrological Processes*, *15*(15), 3011–3023. https://doi.org/10.1002/hyp.388

Caracciolo, D., Noto, L. V., Istanbulluoglu, E., Fatichi, S., & Zhou, X. (2014). Climate change and Ecotone boundaries: Insights from a cellular automata ecohydrology model in a Mediterranean catchment with topography controlled vegetation patterns. *Advances in Water Resources*, *73*, 159–175. https://doi.org/10.1016/j.advwatres.2014.08.001

Cawson, J. G., Sheridan, G. J., Smith, H. G., & Lane, P. N. J. (2012). Surface runoff and erosion after prescribed burning and the effect of different fire regimes in forests and shrublands: A review. *International Journal of Wildland Fire*, *21*(7), 857–872. https://doi.org/10.1071/WF11160

Cawson, J. G., Sheridan, G. J., Smith, H. G., & Lane, P. N. J. (2013). Effects of fire severity and burn patchiness on hillslope-scale surface runoff, erosion and hydrologic connectivity in a prescribed burn. *Forest Ecology and Management*, *310*, 219–233.

This article is protected by copyright. All rights reserved.

Author Manuscript

https://doi.org/10.1016/j.foreco.2013.08.016

Certini, G. (2005). Effects of fire on properties of forest soils: A review. *Oecologia*, *143*(1), 1–10. https://doi.org/10.1007/s00442-004-1788-8

Cheal, D. (2010). *Growth stages and tolerable fire intervals for Victoria's native vegetation data sets. Fire and Adaptive Management. Report No. 84*. Retrieved from https://www.ffm.vic.gov.au/__data/assets/pdf_file/0008/21113/Report-84-REDUCED-SIZE-Growth-Stages-and-Tolerable-Fire-Intervals-For-Victorias-Native-Vegetation-Data-Se.pdf

Clapp, R. B., & Hornberger, G. M. (1978). Empirical equations for some soil hydraulic properties. *Water Resources Research*, *14*(4), 601–604. https://doi.org/10.1029/WR014i004p00601

Clarke, P. J., Lawes, M. J., Murphy, B. P., Russell-Smith, J., Nano, C. E. M., Bradstock, R. A., et al. (2015). A synthesis of postfire recovery traits of woody plants in Australian ecosystems. *Science of the Total Environment*, *534*, 31–42. https://doi.org/10.1016/j.scitotenv.2015.04.002

Cohen, S., Willgoose, G. R., & Hancock, G. (2013). Soil-landscape response to mid and late Quaternary climate fluctuations based on numerical simulations. *Quaternary Research (United States)*, *79*(3), 452–457. https://doi.org/10.1016/j.yqres.2013.01.001

Cohen, S., Willgoose, G. R., & Hancock, G. R. (2009). The mARM spatially distributed soil evolution model: A computationally efficient modeling framework and analysis of hillslope soil surface organization. *Journal of Geophysical Research: Earth Surface (2003–2012)*, *114*(F3). https://doi.org/10.1029/2008JF001214

Coon, W. 1998. (1998). *Estimation of Roughness Coefficients*. *U.S. Geological Survey water-supply paper*. U.S. Geological Survey. Retrieved from https://pubs.er.usgs.gov/publication/wsp2441

Cowpertwait, P. S. P., O'Connell, P. E., Metcalfe, A. V., & Mawdsley, J. A. (1996). Stochastic point process modelling of rainfall. I. Single-site fitting and validation. *Journal of Hydrology*, *175*(1–4), 17–46. https://doi.org/10.1016/S0022-1694(96)80004-7

Czarnota, K., Roberts, G. G., White, N. J., & Fishwick, S. (2014). Spatial and temporal patterns of Australian dynamic topography from river profile modeling. *Journal of Geophysical Research: Solid Earth*, *119*(2), 1384–1424. https://doi.org/10.1002/2013JB010436

DeBano, L. F. (2000). The role of fire and soil heating on water repellency in wildland environments: a review. *Journal of Hydrology*, *231*, 195–206. https://doi.org/10.1016/S0022-1694(00)00194-3

Boyle, M., Frankenberger, W. T., & Stolzy, L. H. (1989). The influence of organic matter on soil aggregation and water infiltration. Journal of Production Agriculture, 2(4), 290–299. https://doi.org/doi:10.2134/jpa1989.0290

DELWP. (2007). Bioregions and EVC Benchmark. Retrieved from https://www.environment.vic.gov.au/biodiversity/bioregions-and-evc-benchmarks

Dietrich, W. E., Bellugi, D. G., Sklar, L. S., Stock, J. D., Heimsath, A. M., & Roering, J. J. (2003). Geomorphic transport laws for predicting landscape form and dynamics. In P. R.

This article is protected by copyright. All rights reserved.

Author Manuscript

Wilcock & R. Iverson (Eds.), *Prediction in geomorphology* (pp. 103–132). Florida, US: AGU.

Donohue, R. J., Roderick, M. L., & McVicar, T. R. (2007). On the importance of including vegetation dynamics in Budyko's hydrological model. *Hydrology and Earth System Sciences*, *11*(2), 983–995. https://doi.org/10.5194/hess-11-983-2007

Donohue, R. J., Roderick, M. L., & McVicar, T. R. (2012). Roots, storms and soil pores: Incorporating key ecohydrological processes into Budyko's hydrological model. *Journal of Hydrology*, *436–437*, 35–50. https://doi.org/10.1016/j.jhydrol.2012.02.033

Fairman, T. A., Nitschke, C. R., & Bennett, L. T. (2016). Too much, too soon? A review of the effects of increasing wildfire frequency on tree mortality and regeneration in temperate eucalypt forests. *International Journal of Wildland Fire*, *25*(8), 831–848. https://doi.org/10.1071/WF15010

Fifield, L. K., Wasson, R. J., Pillans, B., & Stone, J. O. (2010). The longevity of hillslope soil in SE and NW Australia. *Catena*, *81*(1), 32–42. https://doi.org/10.1016/j.catena.2010.01.003

Finkele, K., Mills, G. A., Beard, G., & Jones, D. A. (2006). National gridded drought factors and comparison of two soil moisture deficit formulations used in prediction of Forest Fire Danger Index in Australia. Australian Meteorological Magazine, 55, 183–197.

Fletcher, M. S., Wolfe, B. B., Whitlock, C., Pompeani, D. P., Heijnis, H., Haberle, S. G., et al. (2014a). The legacy of mid-holocene fire on a Tasmanian montane landscape. *Journal of Biogeography*, *41*(3), 476–488. https://doi.org/10.1111/jbi.12229

Fletcher, M. S., Wood, S. W., & Haberle, S. G. (2014b). A fire-driven shift from forest to non-forest: Evidence for alternative stable states? *Ecology*, *95*(9), 2504–2513. https://doi.org/10.1890/12-1766.1

Gabet, E. J., & Dunne, T. (2003). A stochastic sediment delivery model for a steep Mediterranean landscape. *Water Resources Research*, *39*(9). https://doi.org/10.1029/2003WR002341

Gabet, E. J., Reichman, O. J., & Seabloom, E. W. (2003). The effects of bioturbation on soil processes and sediment transport. *Annual Review of Earth and Planetary Sciences*, *31*, 249–273. https://doi.org/10.1146/annurev.earth.31.100901.141314

Gerten, D., Schaphoff, S., Haberlandt, U., Lucht, W., & Sitch, S. (2004). Terrestrial vegetation and water balance - Hydrological evaluation of a dynamic global vegetation model. *Journal of Hydrology*, *286*(1–4), 249–270. https://doi.org/10.1016/j.jhydrol.2003.09.029

Gill, T., Johansen, K., Phinn, S. R., Trevithick, R., Scarth, P., & Armston, J. (2017). A method for mapping Australian woody vegetation cover by linking continental-scale field data and long-term Landsat time series. *International Journal of Remote Sensing*, *38*(3), 679–705. https://doi.org/10.1080/01431161.2016.1266112

Givnish, T., Wond, S. C., Stuart-Williams, H., Holloway-Phillips, M., & Farquhar, G. D. (2014). Determinants of maximum tree height in Eucalyptusspecies along a rainfall gradient in Victoria, Australia. *Ecology*, *95*(11), 2991–3007. https://doi.org/10.1890/14-0240.1

Grierson, P. F., Adams, M. A., & Attiwill, P. M. (1992). Estimates of carbon storage in the aboveground biomass of victoria's forests. *Australian Journal of Botany*, *40*(5), 631–640.

This article is protected by copyright. All rights reserved.

Author Manuscript

https://doi.org/10.1071/BT9920631

Hahm, W. J., Rempe, D. M., Dralle, D. N., Dawson, T. E., Lovill, S. M., Bryk, A. B., et al. (2019). Lithologically Controlled Subsurface Critical Zone Thickness and Water Storage Capacity Determine Regional Plant Community Composition. *Water Resources Research*, *55*(4), 3028–3055. https://doi.org/10.1029/2018WR023760

Hancock, G. R., Hugo, J., Webb, A. A., & Turner, L. (2017). Sediment transport in steep forested catchments – An assessment of scale and disturbance. *Journal of Hydrology*, *547*, 613–622. https://doi.org/10.1016/j.jhydrol.2017.02.022

Heimsath, A. M., Chappell, J., Dietrich, W. E., Nishiizumi, K., & Finkel, R. C. (2001). Late Quaternary erosion in southeastern Australia: A field example using cosmogenic nuclides. *Quaternary International*, *82*(85), 169–185. https://doi.org/10.1016/S1040-6182(01)00038-6

Heimsath, A. M., Dietrich, W. E., Nishiizumi, K., & Finkel, R. C. (1997). The soil production function and landscape equilibrium. *Nature*, *388*(6640), 358–361. https://doi.org/10.1038/41056

Heimsath, A. M., Fink, D., & Hancock, G. R. (2009). The 'humped' soil production function: eroding Arnhem Land, Australia. *Earth Surface Processes and Landforms*, *34*(12), 1674–1684. https://doi.org/https://doi.org/10.1002/esp.1859

Hurteau, M. D., Liang, S., Westerling, A. L., & Wiedinmyer, C. (2019). Vegetation-fire feedback reduces projected area burned under climate change. *Scientific Reports*, *9*(1), 2838. https://doi.org/10.1038/s41598-019-39284-1

Inbar, A., Lado, M., Sternberg, M., Tenau, H., & Ben-Hur, M. (2014). Forest fire effects on soil chemical and physicochemical properties, infiltration, runoff, and erosion in a semiarid Mediterranean region. *Geoderma*, *221–222*, 131–138. https://doi.org/10.1016/j.geoderma.2014.01.015

Inbar, A., Nyman, P., Rengers, F. K., Lane, P. N. J., & Sheridan, G. J. (2018). Climate Dictates Magnitude of Asymmetry in Soil Depth and Hillslope Gradient. *Geophysical Research Letters*, *45*(13), 6514–6522. https://doi.org/10.1029/2018GL077629

Istanbulluoglu, E. (2016). Landscape Evolution Models and Ecohydrologic Processes. In E. A. (Edward A. Johnson & Y. E. Martin (Eds.), *A biogeoscience approach to ecosystems* (pp. 135–179). Cambridge, United Kingdom: Cambridge University Press.

Istanbulluoglu, E., & Bras, R. L. (2005). Vegetation-modulated landscape evolution: Effects of vegetation on landscape processes, drainage density, and topography. *Journal of Geophysical Research: Earth Surface*, *110*(2), 1–19. https://doi.org/10.1029/2004JF000249

Istanbulluoglu, E., & Bras, R. L. (2006). On the dynamics of soil moisture, vegetation, and erosion: Implications of climate variability and change. *Water Resources Research*, *42*(6). https://doi.org/10.1029/2005WR004113

Istanbulluoglu, E., Tarboton, D. G., Pack, R. T., & Luce, C. H. (2004). Modeling of the interactions between forest vegetation, disturbances, and sediment yields. *Journal of Geophysical Research: Earth Surface*, *109*(F1), F01009. https://doi.org/10.1029/2003jf000041

This article is protected by copyright. All rights reserved.

Istanbulluoglu, E., Wang, T., & Wedin, D. A. (2012). Evaluation of ecohydrologic model parsimony at local and regional scales in a semiarid grassland ecosystem. *Ecohydrology*, *5*(1), 121–142. https://doi.org/10.1002/eco.211

Istanbulluoglu, E., Yetemen, O., Vivoni, E. R., Gutiérrez- Jurado, H. A., & Bras, R. L. (2008). Eco-geomorphic implications of hillslope aspect: Inferences from analysis of landscape morphology in central New Mexico. *Geophysical Research Letters*, *35*(14), 1–6. https://doi.org/10.1029/2008GL034477

Jenny, H. (1941). Factors of Soil Formation: A System of Quantitative Pedology. New York: Dover Publication, INC.

Kandel, D. D., Western, A. W., & Grayson, R. B. (2005). Scaling from process timescales to daily time steps: A distribution function approach. *Water Resources Research*, *41*(2), 1–16. https://doi.org/10.1029/2004WR003380

Keith, H., Lindenmayer, D. B., MacKey, B. G., Blair, D. P., Carter, L., McBurney, L. M., et al. (2014). Accounting for biomass carbon stock change due to wildfire in temperate forest landscapes in Australia. *PLoS ONE*, *9*(9). https://doi.org/10.1371/journal.pone.0107126

Keith, H., Mackey, B., Berry, S. L., Lindenmayer, D. B., & Gibbons, P. (2010). Estimating carbon carrying capacity in natural forest ecosystems across heterogeneous landscapes - addressing sources of error. *Global Change Biology*, *16*(11), 2971–2989. https://doi.org/10.1111/j.1365-2486.2009.02146.x

Keith, H., Mackey, B. G., & Lindenmayer, D. B. (2009). Re-evaluation of forest biomass carbon stocks and lessons from the world's most carbon-dense forests. *Proceedings of the National Academy of Sciences of the United States of America*, *106*(28), 11635–11640. https://doi.org/10.1073/pnas.0901970106

Kennedy, A., & Jamieson, D. (2007). Ecological Fire Management in North East Victoria. In *Proceedings of the Joint AFAC/Bushfire CRC Conference* (pp. 18–20).

Klein, T., Randin, C., & Körner, C. (2015). Water availability predicts forest canopy height at the global scale. *Ecology Letters*, *18*(12), 1311–1320. https://doi.org/10.1111/ele.12525

Krawchuk, M. A., & Moritz, M. A. (2011). Constraints on global fire activity vary across a resource gradient. *Ecology*, *92*(1), 121–132. https://doi.org/10.1890/09-1843.1

Krueger, E. S., Ochsner, T. E., Carlson, J. D., Engle, D. M., Twidwell, D., & Fuhlendorf, S. D. (2016). Concurrent and antecedent soil moisture relate positively or negatively to probability of large wildfires depending on season. *International Journal of Wildland Fire*, *25*(2), 257–668. https://doi.org/10.1071/WF15104

Kuczera, G. (1987). Prediction of water yield reductions following a bushfire in ash-mixed species eucalypt forest. *Journal of Hydrology*, *94*(3–4), 215–236. https://doi.org/10.1016/0022-1694(87)90054-0

Laio, F., D'Odorico, P., & Ridolfi, L. (2006). An analytical model to relate the vertical root distribution to climate and soil properties. *Geophysical Research Letters*, *33*(18). https://doi.org/10.1029/2006GL027331

Laio, F., Porporato, A., Ridolfi, L., & Rodriguez-Iturbe, I. (2001). Plants in water-controlled ecosystems: Active role in hydrologic processes and response to water stress: II.

This article is protected by copyright. All rights reserved.

Author Manuscript

Probabilistic soil moisture dynamics. *Advances in Water Resources*, *24*(7), 707–723.

Lane, P. N. J., Croke, J. C., & Dignan, P. (2004). Runoff generation from logged and burnt convergent hillslopes: Rainfall simulation and modelling. *Hydrological Processes*, *18*(5), 879–892. https://doi.org/10.1002/hyp.1316

Lane, P. N. J., Sheridan, G. J., & Noske, P. J. (2006). Changes in sediment loads and discharge from small mountain catchments following wildfire in south eastern Australia. *Journal of Hydrology*, *331*(3–4), 495–510. https://doi.org/10.1016/j.jhydrol.2006.05.035

Langhans, C., Lane, P. N. J., Nyman, P., Noske, P. J., Cawson, J. G., Oono, A., & Sheridan, G. J. (2016a). Scale-dependency of effective hydraulic conductivity on fire-affected hillslopes. *Water Resources Research*, *52*(7), 5041–5055. https://doi.org/10.1002/2016WR018998

Langhans, C., Smith, H. G., Chong, D. M. O., Nyman, P., Lane, P. N. J., & Sheridan, G. J. (2016). A model for assessing water quality risk in catchments prone to wildfire. *Journal of Hydrology*, *534*, 407–426. https://doi.org/10.1016/j.jhydrol.2015.12.048

Lohse, K. A., & Dietrich, W. E. (2005). Contrasting effects of soil development on hydrological properties and flow paths. Water Resources Research, 41(12), 1–17. https://doi.org/10.1029/2004WR003403

McCarthy, M. A., Gill, A. M., & Bradstock, R. A. (2001). Theoretical fire-interval distributions. *International Journal of Wildland Fire*, *10*(1), 73–77. https://doi.org/10.1071/WF01013

McGuire, L. A., Pelletier, J. D., & Roering, J. J. (2014). Development of topographic asymmetry: Insights from dated cinder cones in the western United States. *Journal of Geophysical Research F: Earth Surface*, *119*(8), 1725–1750. https://doi.org/10.1002/2014JF003081

Milodowski, D. T., Mudd, S. M., & Mitchard, E. T. A. (2015). Erosion rates as a potential bottom-up control of forest structural characteristics in the Sierra Nevada Mountains. *Ecology*, *96*(1), 31–38. https://doi.org/10.1890/14-0649.1

Mitchell, P. J., Benyon, R. G., & Lane, P. N. J. (2012). Responses of evapotranspiration at different topographic positions and catchment water balance following a pronounced drought in a mixed species eucalypt forest, Australia. *Journal of Hydrology*, *440–441*, 62–74. https://doi.org/10.1016/j.jhydrol.2012.03.026

Montaldo, N., Rondena, R., Albertson, J. D., & Mancini, M. (2005). Parsimonious modeling of vegetation dynamics for ecohydrologic studies of water-limited ecosystems. *Water Resources Research*, *41*(10). https://doi.org/10.1029/2005WR004094

Moody, J. A., & Martin, D. A. (2001). Initial hydrologic and geomorphic response following a wildfire in the Colorado Front Range. *Earth Surface Processes and Landforms*, *26*(10), 1049–1070. https://doi.org/10.1002/esp.253

Nolan, R. H., Boer, M. M., Resco De Dios, V., Caccamo, G., & Bradstock, R. A. (2016). Large-scale, dynamic transformations in fuel moisture drive wildfire activity across southeastern Australia. *Geophysical Research Letters*, *43*(9), 4229–4238. https://doi.org/10.1002/2016GL068614

Nolan, R. H., Lane, P. N. J., Benyon, R. G., Bradstock, R. A., & Mitchell, P. J. (2014). Changes in evapotranspiration following wildfire in resprouting eucalypt forests. *Ecohydrology*, *7*(5),

This article is protected by copyright. All rights reserved.

1338 1363–1377. https://doi.org/10.1002/eco.1463

1339 Noske, P. J., Nyman, P., Lane, P. N. J., & Sheridan, G. J. (2016). Effects of aridity in controlling
1340 the magnitude of runoff and erosion after wildfire. *Water Resources Research*, *52*, 4338–
1341 4357. https://doi.org/10.1002/2015WR017611

1342 Nyman, P., Baillie, C. C., Duff, T. J., & Sheridan, G. J. (2018). Eco-hydrological controls on
1343 microclimate and surface fuel evaporation in complex terrain. *Agricultural and Forest*
1344 *Meteorology*, *252*, 49–61. https://doi.org/10.1016/j.agrformet.2017.12.255

1345 Nyman, P., Metzen, D., Noske, P. J., Lane, P. N. J., & Sheridan, G. J. (2015). Quantifying the
1346 effects of topographic aspect on water content and temperature in fine surface fuel.
1347 *International Journal of Wildland Fire*, *24*(8), 1129–1142.
1348 https://doi.org/10.1071/WF14195

1349 Nyman, P., Rutherfurd, I. D., Lane, P. N. J., & Sheridan, G. J. (2019). Debris flows in southeast
1350 Australia linked to drought, wildfire, and the El Niño-Southern Oscillation. *Geology*, *47*(5),
1351 491–494. https://doi.org/10.1130/G45939.1

1352 Nyman, P., Sheridan, G. J., & Lane, P. N. J. (2010). Synergistic effects of water repellency and
1353 macropore flow on the hydraulic conductivity of a burned forest soil, south-east Australia.
1354 *Hydrological Processes*, *24*(20), 2871–2887. https://doi.org/10.1002/hyp.7701

1355 Nyman, P., Sheridan, G. J., Moody, J. A., Smith, H. G., Noske, P. J., & Lane, P. N. J. (2013).
1356 Sediment availability on burned hillslopes. *Journal of Geophysical Research: Earth*
1357 *Surface*, *118*(4), 2451–2467. https://doi.org/10.1002/jgrf.20152

1358 Nyman, P., Sheridan, G. J., Smith, H. G., & Lane, P. N. J. (2011). Evidence of debris flow
1359 occurrence after wildfire in upland catchments of south-east Australia. *Geomorphology*,
1360 125(3), 383–401. https://doi.org/10.1016/j.geomorph.2010.10.016

1361 Nyman, P., Sheridan, G. J., Smith, H. G., & Lane, P. N. J. (2014a). Modeling the effects of
1362 surface storage, macropore flow and water repellency on infiltration after wildfire. Journal
1363 of Hydrology, 513, 301–313. https://doi.org/https://doi.org/10.1016/j.jhydrol.2014.02.044

1364 Nyman, P., Sherwin, C. B., Langhans, C., Sheridan, G. J., & Lane, P. N. J. (2014b).
1365 Downscaling regional climate data to calculate the radiative index of dryness in complex
1366 terrain. *Australian Metrological and Oceanographic Journal*, *64*(2), 109–122.
1367 https://doi.org/10.22499/2.6402.003

1368 Olson, J. S. (1963). Energy Storage and the Balance of Producers and Decomposers in
1369 Ecological Systems. *Ecology*, *44*(2), 322–331. https://doi.org/10.2307/1932179

1370 Orem, C. A., & Pelletier, J. D. (2016). The predominance of post-wildfire erosion in the long-
1371 term denudation of the Valles Caldera, New Mexico. *Journal of Geophysical Research F:*
1372 *Earth Surface*, *121*(5), 843–864. https://doi.org/10.1002/2015JF003663

1373 Parks, S. A., Miller, C., Holsinger, L. M., Baggett, L. S., & Bird, B. J. (2016). Wildland fire
1374 limits subsequent fire occurrence. *International Journal of Wildland Fire*, *25*(2), 182–190.
1375 https://doi.org/10.1071/WF15107

1376 Patton, N. R., Lohse, K. A., Godsey, S. E., Crosby, B. T., & Seyfried, M. S. (2018). Predicting
1377 soil thickness on soil mantled hillslopes. *Nature Communications*, *9*(1), 3329.
1378 https://doi.org/10.1038/s41467-018-05743-y

Author Manuscript

This article is protected by copyright. All rights reserved.

Pausas, J. G., & Bradstock, R. A. (2007). Fire persistence traits of plants along a productivity and disturbance gradient in mediterranean shrublands of south-east Australia. *Global Ecology and Biogeography*, *16*(3), 330–340. https://doi.org/10.1111/j.1466-8238.2006.00283.x

Pelletier, J. D., Barron-Gafford, G. A., Breshears, D. D., Brooks, P. D., Chorover, J., Durcik, M., et al. (2013). Coevolution of nonlinear trends in vegetation, soils, and topography with elevation and slope aspect: A case study in the sky islands of southern Arizona. *Journal of Geophysical Research:Earth Surface*, *118*(2), 741–758. https://doi.org/Doi 10.1002/Jgrf.20046

Pelletier, J. D., Barron-Gafford, G. A., Gutiérrez- Jurado, H. A., Hinckley, E. S., Istanbulluoglu, E., McGuire, L. A., et al. (2018). Which way do you lean? Using slope aspect variations to understand Critical Zone processes and feedbacks. *Earth Surface Processes and Landforms*, *43*(5), 1133–1154. https://doi.org/10.1002/esp.4306

Phillips, J. D. (2010). The convenient fiction of steady-state soil thickness. *Geoderma*, *156*(3–4), 389–398. https://doi.org/10.1016/j.geoderma.2010.03.008

Porder, S. (2014). Coevolution of life and landscapes. *Proceedings of the National Academy of Sciences of the United States of America*, *111*(9), 3207–3208. https://doi.org/10.1073/pnas.1400954111

Prentice, I. C., Kelley, D. I., Foster, P. N., Friedlingstein, P., Harrison, S. P., & Bartlein, P. J. (2011). Modeling fire and the terrestrial carbon balance. *Global Biogeochemical Cycles*, *25*(3). https://doi.org/10.1029/2010GB003906

Priestley, C., & Taylor, R. (1972). On the Assessment of Surface Heat Flux and Evaporation Using Large-Scale Parameters'. *Monthly Weather Review*, *100*(2), 81–92. https://doi.org/https://doi.org/10.1175/1520-0493(1972)100<0081:OTAOSH>2.3.CO;2

Prosser, I. P., & Williams, L. (1998). The effect of wildfire on runoff and erosion in native Eucalyptus forest. *Hydrological Processes*, *12*(2), 251–265. https://doi.org/https://doi.org/10.1002/(SICI)1099-1085(199802)12:2<251::AID-HYP574>3.0.CO;2-4

Rasmussen, C., Pelletier, J. D., Troch, P. A., Swetnam, T. L., & Chorover, J. (2015). Quantifying Topographic and Vegetation Effects on the Transfer of Energy and Mass to the Critical Zone. *Vadose Zone Journal*, *14*(11). https://doi.org/10.2136/vzj2014.07.0102

Rees, D. B. (1982). *A study of soils in the Reefton experimental area; with particular reference to hydrological properties*. Melbourne, Australia. Retrieved from http://vro.agriculture.vic.gov.au/dpi/vro/portregn.nsf/pages/port_soil_surveys_reefton

Riebe, C. S., Riebe, J., Kirchner, R., & Finkel, R. C. (2004). Erosional and climatic effects on long-term chemical weathering rates in granitic landscapes spanning diverse climate regimes. *Earth and Planetary Science Letters*, *224*(3), 547–562. https://doi.org/https://doi.org/10.1016/j.epsl.2004.05.019

Rodriguez-Iturbe, I. (2000). Ecohydrology : A hydrologic perspective of climate-soil-vegetation dynamics. *Water Resources Research*, *36*(1), 3–9. https://doi.org/https://doi.org/10.1029/1999WR900210

Rodriguez-Iturbe, I., Febres De Power, B., & Valdes, J. B. (1987). Rectangular pulses point

This article is protected by copyright. All rights reserved.

Author Manuscript

process models for rainfall: analysis of empirical data. Journal of Geophysical Research, 92(D8), 9645–9656. https://doi.org/10.1029/JD092iD08p09645

Rodriguez-Iturbe, I., D'Odorico, P., Porporato, A., & Ridolfi, L. (1999a). On the spatial and temporal links between vegetation, climate, and soil moisture. *Water Resources Research, 35*(12), 3709–3722. https://doi.org/10.1029/1999WR900255

Rodriguez-Iturbe, I., Porporato, A., Ridolfi, L., Isham, V., & Cox, D. R. (1999b). Probabilistic modelling of water balance at a point: the role of climate, soil and vegetation. *Proceedings of the Royal Society of London. Series A: Mathematical, Physical and Engineering Sciences, 455*, 3789–3805. https://doi.org/10.1098/rspa.1999.0477

Roering, J. J. (2008). How well can hillslope evolution models "explain" topography? Simulating soil transport and production with high-resolution topographic data. *Bulletin of the Geological Society of America, 120*(9–10), 1248–1262. https://doi.org/10.1130/B26283.1

Roering, J. J., & Gerber, M. (2005). Fire and the evolution of steep, soil-mantled landscapes. *Geology, 33*(5), 349–352. https://doi.org/10.1130/G21260.1

Roering, J. J., Kirchner, J. W., & Dietrich, W. E. (1999). Evidence for nonlinear, diffusive sediment transport on hillslopes and implications for landscape morphology. *Water Resources Research, 35*(3), 853–870. https://doi.org/10.1029/1998WR900090

Roering, J. J., Marshall, J., Booth, A. M., Mort, M., & Jin, Q. (2010). Evidence for biotic controls on topography and soil production. *Earth and Planetary Science Letters, 298*(1–2), 183–190. https://doi.org/10.1016/j.epsl.2010.07.040

Saxton, K. E., & Rawls, W. J. (2006). Soil Water Characteristic Estimates by Texture and Organic Matter for Hydrologic Solutions. *Soil Science Society of America Journal, 70*(5), 1569. https://doi.org/10.2136/sssaj2005.0117

Schwanghart, W., & Scherler, D. (2014). Short Communication: TopoToolbox 2–MATLAB-based software for topographic analysis and modeling in Earth surface sciences. *Earth Surface Dynamics, 2*(1), 1–7. https://doi.org/10.5194/esurf-2-1-2014

Shakesby, R. A., & Doerr, S. H. (2006). Wildfire as a hydrological and geomorphological agent. *Earth-Science Reviews, 74*(3–4), 269–307. https://doi.org/10.1016/j.earscirev.2005.10.006

Sheridan, G. J., Lane, P. N. J., & Noske, P. J. (2007). Quantification of hillslope runoff and erosion processes before and after wildfire in a wet Eucalyptus forest. *Journal of Hydrology, 343*(1), 12–28. https://doi.org/10.1016/j.jhydrol.2007.06.005

Sheridan, G. J., Nyman, P., Langhans, C., Cawson, J. G., Noske, P. J., Oono, A., et al. (2015). Is aridity a high-order control on the hydro-geomorphic response of burned landscapes? *International Journal of Wildland Fire, 25*(3), 262–267. https://doi.org/10.1071/WF14079

Small, E. E. (2005). Climatic controls on diffuse groundwater recharge in semiarid environments of the southwestern United States. *Water Resources Research, 41*(4), 1–17. https://doi.org/10.1029/2004WR003193

Smith, H. G., Sheridan, G. J., Lane, P. N. J., & Bren, L. J. (2011a). Wildfire and salvage harvesting effects on runoff generation and sediment exports from radiata pine and eucalypt forest catchments, south-eastern Australia. *Forest Ecology and Management, 261*(3), 570–

This article is protected by copyright. All rights reserved.

Author Manuscript

581. https://doi.org/10.1016/j.foreco.2010.11.009

Smith, H. G., Sheridan, G. J., Lane, P. N. J., Noske, P. J., & Heijnis, H. (2011b). Changes to sediment sources following wildfire in a forested upland catchment, southeastern Australia. *Hydrological Processes*, *25*(18), 2878–2889. https://doi.org/10.1002/hyp.8050

Smith, H. G., Sheridan, G. J., Nyman, P., Child, D. P., Lane, P. N. J., Hotchkis, M. A. C., & Jacobsen, G. E. (2012). Quantifying sources of fine sediment supplied to post-fire debris flows using fallout radionuclide tracers. *Geomorphology*, *139–140*, 403–415. https://doi.org/10.1016/j.geomorph.2011.11.005

Specht, R. L., & Wood, J. G. (1972). *The vegetation of South Australia: handbook of the flora and fauna of South Australia* (2nd). Adelaide, Ausralia: Government Print.

Stern, H., de Hoedt, G., & Ernst, J. (2000). Objective classification of Australian climates. *Australian Meteorological Magazine*, *49*(2), 87–96.

Tarpanelli, A., Franchini, M., Brocca, L., Camici, S., Melone, F., & Moramarco, T. (2012). A simple approach for stochastic generation of spatial rainfall patterns. *Journal of Hydrology*, *472*, 63–76. https://doi.org/10.1016/j.jhydrol.2012.09.010

Taufik, M., Torfs, P. J. J. F., Uijlenhoet, R., Jones, P. D., Murdiyarso, D., & Van Lanen, H. A. J. (2017). Amplification of wildfire area burnt by hydrological drought in the humid tropics. *Nature Climate Change*, *7*(6), 428–431. https://doi.org/10.1038/nclimate3280

Temme, A. J. A. M., & Vanwalleghem, T. (2016). LORICA – A new model for linking landscape and soil profile evolution: Development and sensitivity analysis. *Computers & Geosciences*, *90*, 131–143. https://doi.org/10.1016/j.cageo.2015.08.004

Temme, A. J. A. M., & Veldkamp, A. (2009). Multi- process Late Quaternary landscape evolution modelling reveals lags in climate response over small spatial scales. *Earth Surface Processes and Landforms*, *34*(4), 573–589.

Tern AusCover. (2017). Australian woody vegetation cover. Retrieved September 18, 2017, from http://auscover.org.au/purl/landsat-persistent-green-2000-2010

Thonicke, K., Spessa, A., Prentice, I. C., Harrison, S. P., Dong, L., & Carmona-Moreno, C. (2010). The influence of vegetation, fire spread and fire behaviour on biomass burning and trace gas emissions: Results from a process-based model. *Biogeosciences*, *7*(6), 1991–2011. https://doi.org/10.5194/bg-7-1991-2010

Thonicke, K., Venevsky, S., Sitch, S., & Cramer, W. (2001). The role of fire disturbance for global vegetation dynamics: Coupling fire into a dynamic global vegetation model. *Global Ecology and Biogeography*, *10*(6), 661–677. https://doi.org/10.1046/j.1466-822X.2001.00175.x

Timbal, B., Ekström, M., Fiddes, S. L., Grose, M. R., Kirono, D., Lim, E.-P., et al. (2016). *Climate change science and Victoria*. Melbourne, Victoria. Retrieved from http://www.cawcr.gov.au/projects/vicci/wp-content/uploads/2016/05/BRR-014.pdf

Trancoso, R., Larsen, J. R., McAlpine, C. A., McVicar, T. R., & Phinn, S. R. (2016). Linking the Budyko framework and the Dunne diagram. *Journal of Hydrology*, *535*(February), 581–597. https://doi.org/10.1016/j.jhydrol.2016.02.017

Author Manuscript

This article is protected by copyright. All rights reserved.

Troch, P. A., Lahmers, T., Meira, A., Mukherjee, R., Pedersen, J. W., Roy, T., & Valdés-Pineda, R. (2015). Catchment coevolution: A useful framework for improving predictions of hydrological change? *Water Resources Research*, *51*(7), 4903–4922. https://doi.org/10.1002/2015WR017032

Tucker, G. E., & Hancock, G. R. (2010). Modelling Landscpae evolution. *Earth Surface Processes and Landforms*, *50*(1), 28–50. https://doi.org/10.1002/esp

van Breemen, N. (1993). Soils as biotic constructs favouring net primary productivity. *Geoderma*. https://doi.org/10.1016/0016-7061(93)90002-3

Van der Sant, R. E., Nyman, P., Noske, P. J., Langhans, C., Lane, P. N. J., & Sheridan, G. J. (2018). Quantifying relations between surface runoff and aridity after wildfire. *Earth Surface Processes and Landforms*, *43*(10), 2033–2044. https://doi.org/10.1002/esp.4370

Vertessy, R. A., Watson, F. G. R., & O'Sullivan, S. K. (2001). Factors determining relations between stand age and catchment water balance in mountain ash forests. *Forest Ecology and Management*, *143*(1–3), 13–26. https://doi.org/10.1016/S0378-1127(00)00501-6

Volkova, L., Bi, H., Murphy, S., & Weston, C. J. (2015). Empirical Estimates of Aboveground Carbon in Open Eucalyptus Forests of South-Eastern Australia and Its Potential Implication for National Carbon Accounting. *Forests*, *6*(10), 3395–3411. https://doi.org/10.3390/f6103395

Wagenbrenner, J. W., Robichaud, P. R., & Elliot, W. J. (2010). Rill erosion in natural and disturbed forests: 2. Modeling approaches. *Water Resources Research*, *46*(10). https://doi.org/10.1029/2009WR008314

Walker, J. (1981). Fuel dynamics in Australian vegetation. In A. M. Gill, R. H. Groves, & I. R. Noble (Eds.), *Fire and the Australian biota* (pp. 101–127). Canberra: Australian Academy of Science.

Walsh, S. F., Nyman, P., Sheridan, G. J., Baillie, C. C., Tolhurst, K. G., & Duff, T. J. (2017). Hillslope-scale prediction of terrain and forest canopy effects on temperature and near-surface soil moisture deficit. *International Journal of Wildland Fire*, *26*(3), 191–208. https://doi.org/10.1071/WF16106

Walther, S. C., Roering, J. J., Almond, P. C., & Hughes, M. W. (2009). Long-term biogenic soil mixing and transport in a hilly, loess-mantled landscape: Blue Mountains of southeastern Washington. *Catena*, *79*(2), 170–178. https://doi.org/10.1016/j.catena.2009.08.003

Waring, R. H., Landsberg, J. J., & Williams, M. (1998). Net primary production of forests: A constant fraction of gross primary production? *Tree Physiology*, *18*(2), 129–134. https://doi.org/10.1093/treephys/18.2.129

Wellman, P. (1987). Eastern highlands of Australia; their uplift and erosion. *Journal of Australian Geology & Geophysics*, *10*, 277–286.

Western, A. W., Grayson, R. B., Blöschl, G., Willgoose, G. R., & McMahon, T. A. (1999). Observed spatial organization of soil moisture and its relation to terrain indices. *Water Resources Research*, *35*(3), 797–810. https://doi.org/10.1029/1998WR900065

Whitehead, D., & Beadle, C. L. (2004). Physiological regulation of productivity and water use in Eucalyptus: A review. *Forest Ecology and Management*, *193*(1–2), 113–140.

This article is protected by copyright. All rights reserved.

Author Manuscript

https://doi.org/10.1016/j.foreco.2004.01.026

Willgoose, G. R., Bras, R. L., & Rodriguez-Iturbe, I. (1991). A coupled channel network growth and hillslope evolution model: 1. Theory. *Water Resources Research, 27*(7), 1671–1684. https://doi.org/10.1029/91WR00935

Williams, C. A., & Albertson, J. D. (2005). Contrasting short- and long-timescale effects of vegetation dynamics on water and carbon fluxes in water-limited ecosystems. *Water Resources Research*, *41*(6), 1–13. https://doi.org/10.1029/2004WR003750

Yetemen, O., Istanbulluoglu, E., Flores-Cervantes, J. H., Vivoni, E. R., & Bras, R. L. (2015). Ecohydrologic role of solar radiation on landscape evolution. *Water Resources Research*, *51*(2), 1127–1157. https://doi.org/10.1002/2014WR016169

Yue, C., Ciais, P., Cadule, P., Thonicke, K., Archibald, S., Poulter, B., et al. (2014). Modelling the role of fires in the terrestrial carbon balance by incorporating SPITFIRE into the global vegetation model ORCHIDEE - Part 1: Simulating historical global burned area and fire regimes. *Geoscientific Model Development*, *7*(6), 2747–2767. https://doi.org/10.5194/gmd-7-2747-2014

Zhang, L., Hickel, K., Dawes, W. R., Chiew, F. H. S., Western, A. W., & Briggs, P. R. (2004). A rational function approach for estimating mean annual evapotranspiration. *Water Resources Research*, *40*(2). https://doi.org/10.1029/2003WR002710

Zhou, X., Istanbulluoglu, E., & Vivoni, E. R. (2013). Modeling the ecohydrological role of topography on tree-grass-shrub coexistence in a semiarid climate. Water Resources Research, 49(206), 2872–2895. https://doi.org/https://doi.org/10.1002/wrcr.20259

Author Manuscript

This article is protected by copyright. All rights reserved.

1564 **Tables**

1565

1566 Table 1 – Model parameters

Notation	Description	Units	Value	Source
	Topography			
S	Slope gradient	m m^{-1}	0.52	Text S8 in supporting information
S_{50}, S_{30}	Slope gradient at 50 and 30 m down the slope, respectively	m m^{-1}	0.52, 0.48	Supporting information (Text S8)
	Climate			
E_s	E_s is a factor reducing E_p to achieve maximum soil evaporation	-	0.7	(Zhou et al., 2013)
L_T	The lag between peak E_p and peak solar forcing	days	30	Estimated
α_{PT}	Priestley & Taylor scalar	-	1.26	(Priestley & Taylor, 1972)
	Soil properties and soil depth balance			
a_{NC}	Constant for calculating the proportion of the NC material transported	-	1.16	(Nyman et al., 2013)
b_{NC}	Constant for calculating the proportion of the NC material transported	-	0.34	(Nyman et al., 2013)
b_{ret}	Water retention parameter	-	4.9	(Zhou et al., 2013)
E_w	Scalar for evaporation rate form soil under wilting point	-	0.1	(Laio et al., 2006)
$H_{NC_{max}}$	Maximum depth of the NC layer	mm	8	(Nyman et al., 2013)
H^*	Exponential folding depth of the soil production rate	m^{-1}	0.5	(Amundson et al., 2015)
K_e	Detachment limited erosivity	h m^{-1}	5.4e^{-3}	(Wagenbrenner et al., 2010)
K_s	Saturated hydraulic conductivity	mm h^{-1}	200	Estimated for porous soil

Author Manuscript

This article is protected by copyright. All rights reserved.

Author Manuscript

m_{st}	Empirical constant in manning's equation	-	0.7	(Istanbulluoglu & Bras, 2005; Willgoose et al., 1991)
n	Porosity (for clay loam)	-	0.5	(Clapp & Hornberger, 1978)
n_{st}	Empirical constant in manning's equation	-	0.6	(Istanbulluoglu & Bras, 2005; Willgoose et al., 1991)
n_T	Manning's roughness coefficient	-	0.022	Estimated as cohesive river bed (Table 3 in Coon, 1998)
s_h	Soil saturation ratio at hygroscopic capacity	-	0.1	(Clapp & Hornberger, 1978)
S_c	Critical gradient above which hillslope diffusion becomes infinite	m m^{-1}	1.25	(Roering, 2008)
s_{cut}	Soil moisture deficit flammability threshold value	-	0.39	Calibrated; Text S5 in supporting information
s_{fc}	Soil saturation ratio at field capacity	-	0.64	(Clapp & Hornberger, 1978)
s_h	Soil saturation ratio at hygroscopic capacity	-	0.1	(Caracciolo et al., 2014)
s_i	Soil saturation ratio at incipient stomata closure	-	0.5	Estimated
s_w	Soil saturation ratio at wilting point	-	0.36	(Clapp & Hornberger, 1978)
β_r	Root density exponential decay term	m^{-1}	2.6	(Roering, 2008)
ε_o	Maximum soil production rate at zero soil depth	m d^{-1}	1.85e^{-7}	(Heimsath et al., 2001)
η	Maximum transport coefficient	m^2 d^{-1}	4.5e^{-3}	(Roering, 2008)
ρ_r	Density of bedrock	kg m^{-3}	2650	
ρ_s	Density of soil	kg m^{-3}	1325	
τ_{crit}	Critical shear stress	Pa	0	(Wagenbrenner et al., 2010)
Vegetation properties and biomass balance				

This article is protected by copyright. All rights reserved.

a_{kss}	Exponent for structural biomass turnover coefficient	-	20	Calibrated
c_{kss}	Exponent for structural biomass turnover coefficient	-	0.55	Calibrated
k_{lp}	leaf production rate	d^{-1}	0.001	Calibrated
k_{sl}	Leaf senescence coefficient	1	$5e^{-5}$	Calibrated
LAI_{gmax}	Maximum LAI for the domain	$m\ m^{-1}$	4.17	Calibrated
M	coefficient for leaf biomass recovery	-	4	Calibrated
m_1	Exponent for maximum biomass	-	0.43	Calibrated
m_2	Exponent for maximum biomass	-	1.79	Calibrated
m_3	Exponent for maximum LAI	-	$4.4e^{-5}$	Calibrated
S_{LAI}	Volume storage per unit LAI	$mm\ LAI_1^{-}$	1	Calibrated
SLA	Specific leaf area	$LAI\ kg^{-1}$	4	(Whitehead & Beadle, 2004)
WUE	Water use efficiency	$kg_{CO2}\ kg_{H2O}^{-1}$	$5e^{-3}$	(Zhou et al., 2013)
α_B	System maximum biomass	$kg\ m^{-2}$	69.11	Calibrated
μ	The ratio between net and gross primary productivity	-	0.47	(Waring et al., 1998)
ω	Conversion ratio of CO_2 to dry matter	$kg_{DM}\ kg_{CO2}^{-1}$	0.55	(Zhou et al., 2013)
	Flammability and fire			
κ_f	Slope of probability reduction	-	$14.7e^{-2}$	Calibrated; Text S5 in supporting information
δ	Maximum fire probability	yr^{-1}	$1.5e^{-3}$	Calibrated; Text S5 in supporting information

1567
1568

Author Manuscript

This article is protected by copyright. All rights reserved.

Table 2- Aridity of the eight climatic scenarios used for model simulations. MAP is mean annual precipitation.

MAP	Aridity (North facing)	Aridity (South facing)
mm	(-)	(-)
721	2.61	1.83
942	2.00	1.40
1261	1.49	1.05
1610	1.17	0.82

Table 3 – Published sources of measured sediment yield

Location	Source	MAP	Type	Time since fire	mean sediment yield reported
		mm		years	t ha^{-1} yr^{-1}
Stoney Gully	Noske et al. (2016)	954	small headwater	1	10.05
				5	0.12
Upper Yarra Catchment	Cawson et al. (2013)	1200	hillslope/ unbound plot	1	0.19
				unburnt	$1.3e^{-4}$
Ella creek	Smith et al. (2011a)	1400	catchment	2	0.11
				unburnt	0.01
East Kiewa	Lane et al. (2006)	1800	catchment	1	2.96
				unburnt	0.23

Author Manuscript

This article is protected by copyright. All rights reserved.

Table 4 - Mean sediment yield after fire and in unburnt state for simulations driven by four different climatic scenarios (Table 2). Values for were based on a 100 kyr simulation for each of the sites.

MAP	Aspect	Aridity	Time since fire	mean post-fire sediment yield[*1]	Modelled fire interval	Denudation rate
mm				$t\ ha^{-1}yr^{-1}$	yr	$mm\ kyr^{-1}$
722	North	2.61	1	8.51	19	83.4
			Unburnt	0.44		
	South	1.86	1	8.53	24	75.4
			unburnt	0.42		
943	North	2	1	8.75	22	87.7
			Unburnt	0.5		
	South	1.4	1	2.62	42	21.1
			Unburnt	0.04		
1261	North	1.49	1	7.89	34	48.2
			unburnt	0.22		
	South	1.05	1	0.2	66	14.0
			Unburnt	$2e^{-3}$		
1611	North	1.17	1	1.5	54	15.7
			Unburnt	$3e^{-3}$		
	South	0.82	1	0.02	89	13.8
			Unburnt	$3e^{-3}$		

[*1] Calculated from first year after each fire event.

Author Manuscript

This article is protected by copyright. All rights reserved.

Figure Captions

Figure 1 –(a) Conceptual model that describes the coevolution of a coupled soil-vegetation system; and (b) a schematic representation of what eco-hydro-geomorphic processes represented in CoolFlameS, are the manner in which they are coupled. The dynamics of soil depth (H), soil moisture (nHs, where s is degree of saturation and n is porosity) and standing biomass (B) are expressed by equations 2-4. Thick coloured arrows represent fluxes of water- (blue), energy- (yellow), carbon- (green) and minerals- (brown). Thin dashed arrows point to the effects of soil moisture on fire and the effect of individual fire on forest cover and soil surface properties. An illustration of the spatial representation of the model system is presented in (c). The system surface area is divided horizontally into vegetated (V_c) and bare ($1 - V_c$) proportions. The vegetated area is further divided into covered (LAI_r) and uncovered ($1 - LAI_r$) proportions. both variables depend are modelled dynamically and depend on the LAI_l using equation 5.

Figure 2 – Map of SE Australia showing the locations of sites that were used for: (i) model grounding (Text S7; Table S5); (ii) the calibration of the Nyman Scott Rectangular Pulse (NSRP) model (Text S1); and (iii) model evaluation.

Figure 3 – Modelled and measured number of days that degree of saturation (s) was above (a and b) and below (c and d) incipient stomata closure; and below the flammability threshold value (e and f), as a function of aridity (left column) and mean annual precipitation (right column). Modelled results display annual value of each metric for 1 kyr simulations as a function of the simulated climatic forcings for the same year (Table 2). For each modelled value, 100-year aridity ($\overline{AI}_{100}$) was calculated as the ratio between mean evaporative demand to mean rainfall for the previous 100 years, starting from year 101. Measured results were calculated from a year-long monitoring of six sites (Table S6).

Figure 4 – comparison of literature to modelled values for: transpiration, soil evaporation and interception loss as a proportion of ET (a); and transpiration, soil evaporation, interception loss and recharge (P-ET) as a proportion of P (b). Modelled results displayed are for simulation running south-facing (SF) wet, north-facing (NF) wet and NF damp climatic scenarios (Table 2), which are compared to measurements described in Vertessy et al. (2001), Nolan et al. (2014) and Mitchell et al. (2012), respectively.

Figure 5 –Distributions of fire return interval (a-c) and the cumulative number of days below soil moisture deficit threshold ($\bar{s}$) for 100 kyr-long simulation forced with (a) dry (red; aridity=2.61), (b) damp (blue; aridity=1.49) and (c) wet (black; aridity=0.82) climatic scenarios (Table 2). $\bar{s}$ is used here as a proxy for flammability and is calculated using Eqn. S8.

Figure 6 – Mean modelled and measured event-scale runoff ratio (SRR) for first year after fire as a function of aridity (a); and measured and modelled discharge for the first year after a fire, as a function of rainfall depth. Modelled values at each aridity point presented in (a) are mean SRR that were calculated using surface runoff that originated only from rainstorms that exceeded a 5 mm h^{-1} threshold (grey markers). The dashed line is a function fitted to measured event-based runoff ratio from 8 meter plots for the range 0.65<aridity<1.80 (Eqn 3 in Van der Sant et al.,

This article is protected by copyright. All rights reserved.

Author Manuscript

2018). Modelled data represent values for 50 m hillslope stretch; Dashed line in (b) is a linear function fitted to measured data.

Figure 7- modelled (H_{ss} and V_{c-ss}) and observed soil depth and projected vegetation cover as a function of aridity for: (a-b) simulations with ($+fire$) and without fire ($-fire$); and for simulations with fire but without post-fire changes in: (c-d) infiltration capacity ($-\Delta I_c$); (e-f) soil cohesiveness ($-\Delta CO$); and (g-h) canopy cover ($-\Delta LAI$). The figure presents results for experiment 1 (a-b) and 2 (c-h). H_{ss} and V_{c-ss} values are plotted over functions and 95% confidence interval (grey area) fitted to soil depth measurements (Inbar et al., 2018) and Remotely sensed vegetation cover using annual LANDSAT values (Tern AusCover, 2017) for areas near the three steepest sites (Table S5). Confidence interval for vegetation cover was generated for 1,000 randomly sampled values of remotely sensed vegetation cover.

Figure 8 - The coevolution of soil depth (H); projected vegetation cover (V_c); and fire return interval (FRI) with time (a-c); and their values plotted within a 2D space (d) for simulations with (full circular markers) and without fire (empty green triangular markers). Simulations used in this analysis were driven by dry climate which was interrupted by a 150 kyr long wet period. Climate changes from dry-to-wet and from wet-to-dry in (a-c) are marked by red and blue triangles (respectively). Each circular marker in (d) represents the mean value for V_c and H calculated for 1000 yearlong bins. For simulation with fire (d), size and color of each circular marker represent the mean FRI for the same period. To include the element of time in (d), simulation starting and end points are marked with a cross and a plus sign (respectively), and years 10k, 11k, 160k, 161k and 200k are marked with appropriate text.

Figure 9 – Climatically-driven feedback between soil moisture, fire return interval (FRI), fluvial erosion and soil depth. Red arrows represent effects that are related to fire and green arrows those that are not. In this feedback, long-term change in climate affects soil moisture, vegetation cover and fire frequency. This, in-turn force changes on soil depth and its water holding capacity by altering the rate of fluvial erosion, which feeds back to soil moisture, vegetation cover and fire frequency.

Author Manuscript

This article is protected by copyright. All rights reserved.

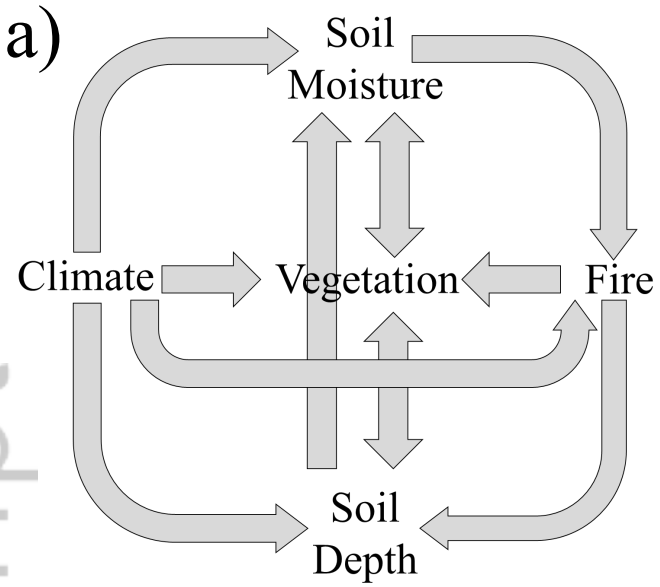

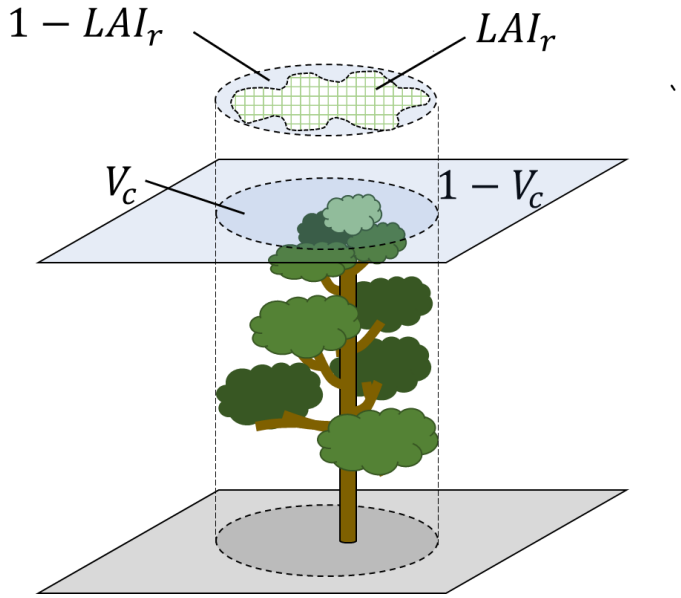

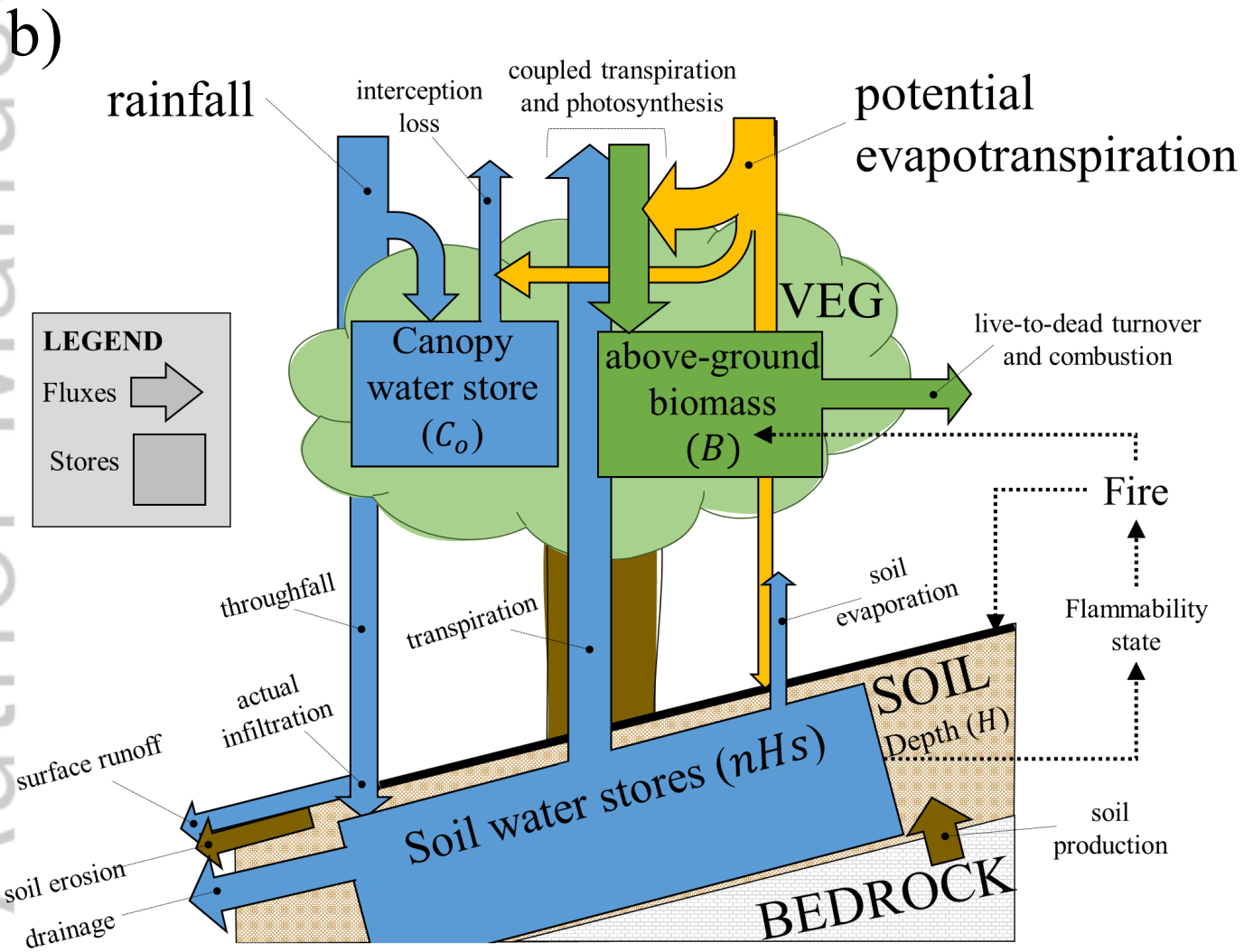

Author Manuscript

This article is protected by copyright. All rights reserved.

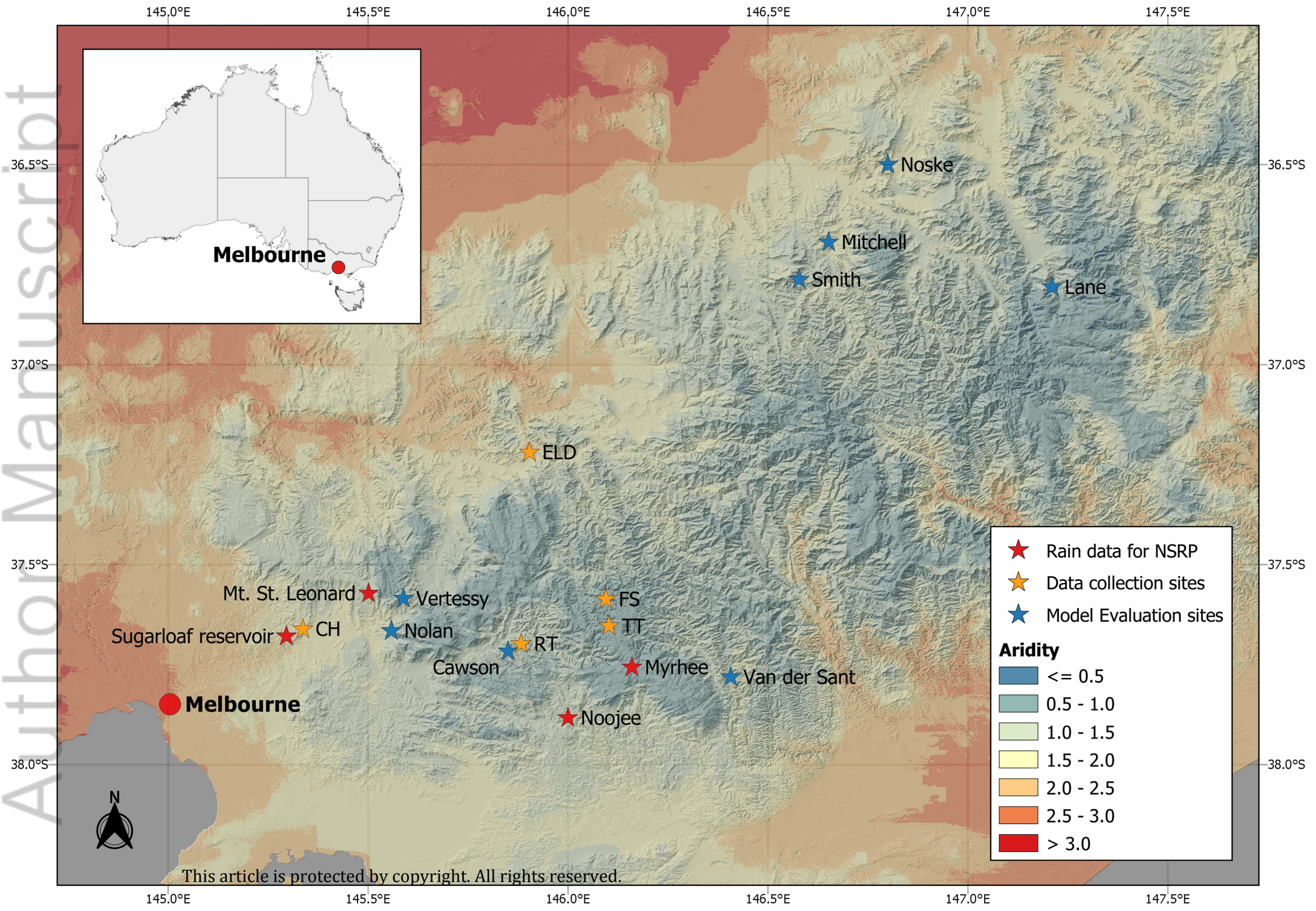

Author Manuscript

This article is protected by copyright. All rights reserved.

Author Manuscript

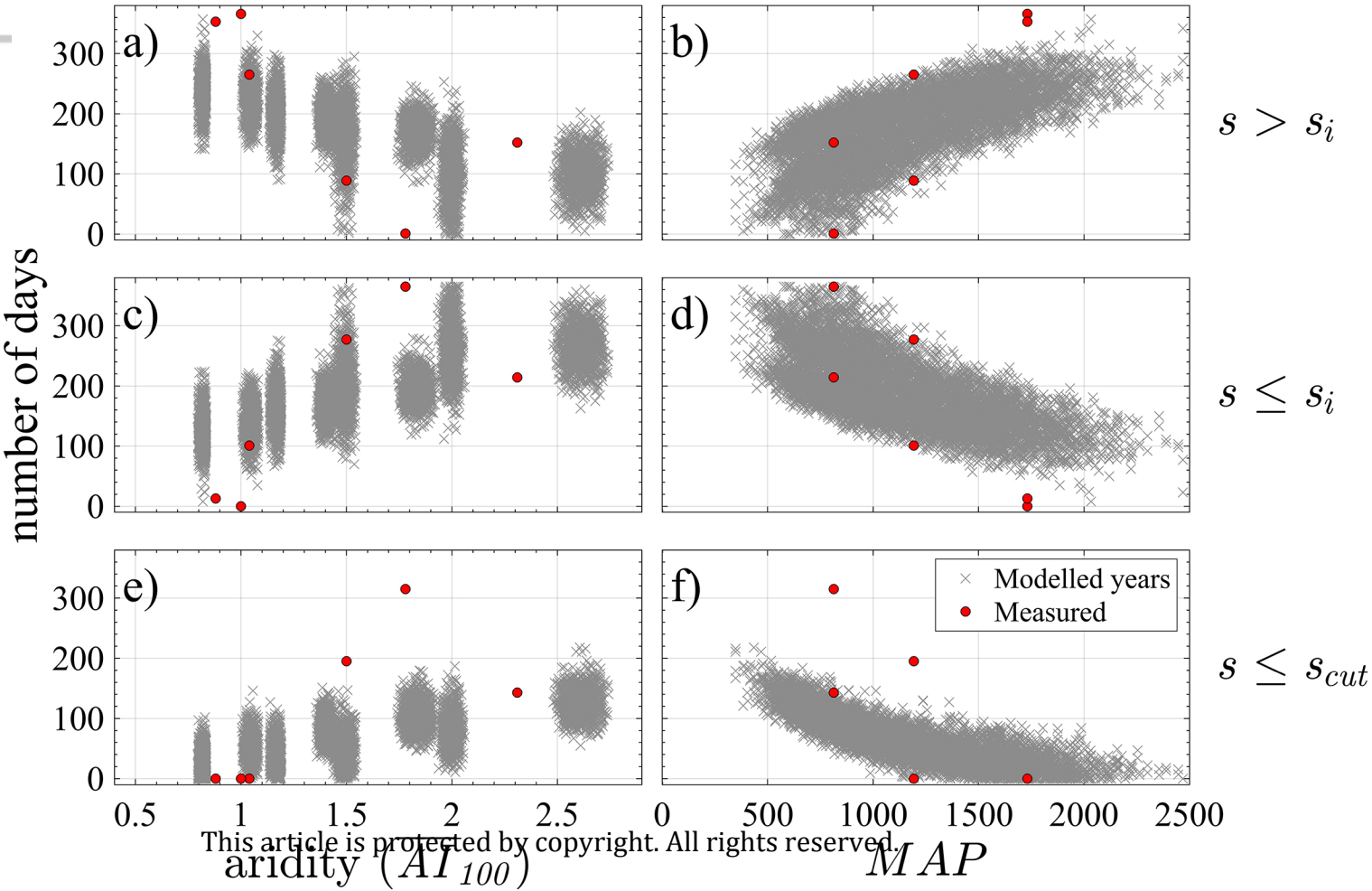

This article is protected by copyright. All rights reserved.

Author Manuscript

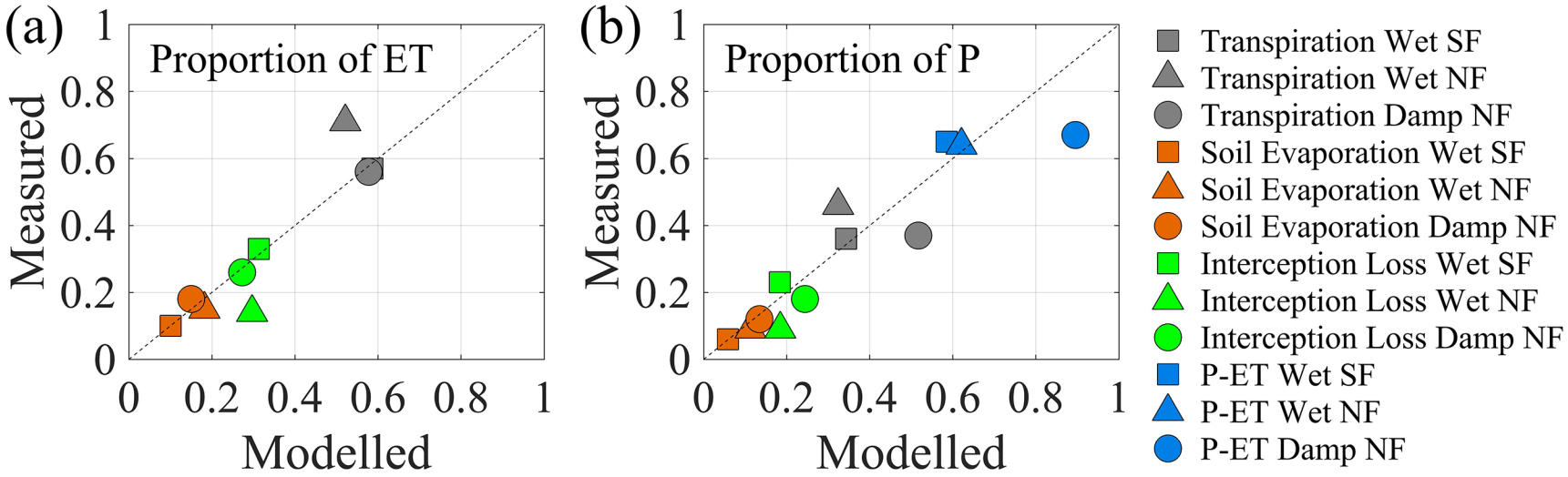

This article is protected by copyright. All rights reserved.

Author Manuscript

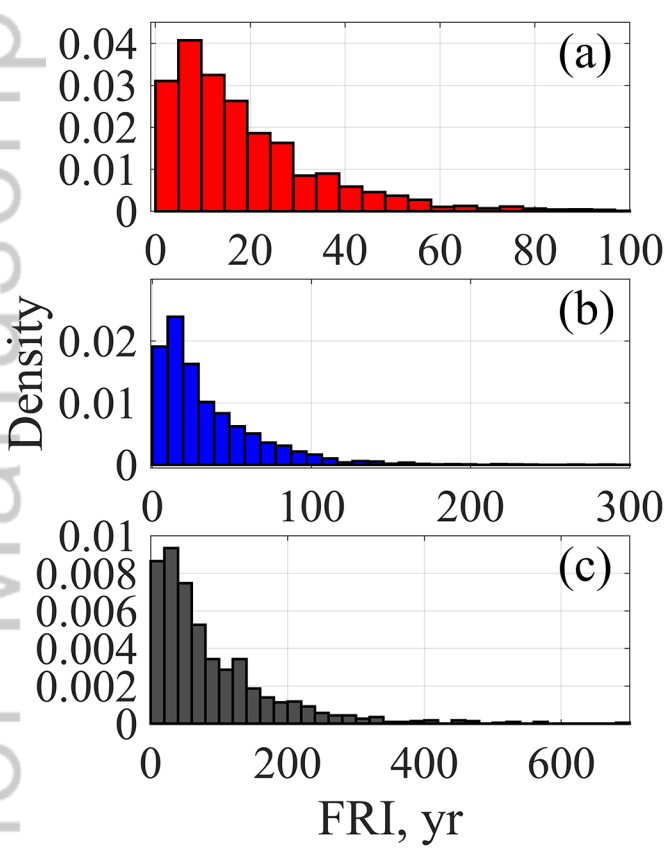

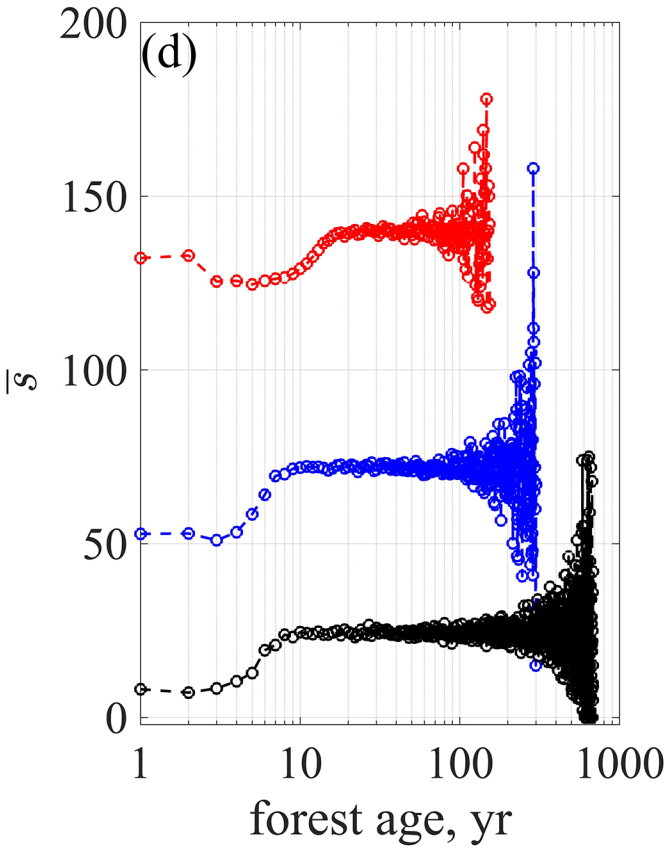

This article is protected by copyright. All rights reserved.

Author Manuscript

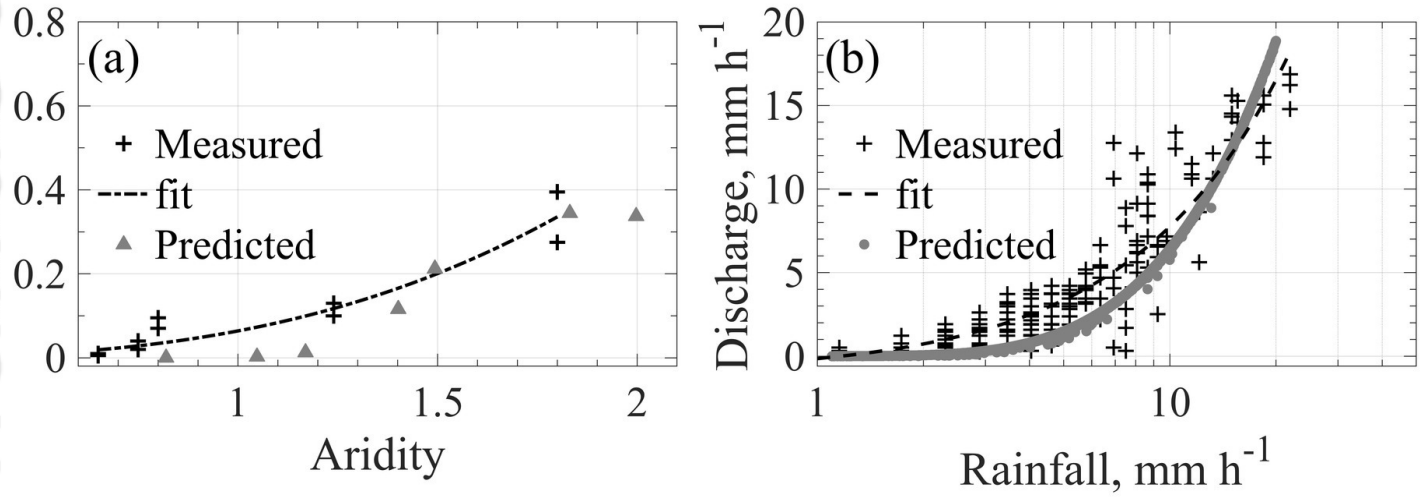

2019WR026005-f06-z-.jpg

This article is protected by copyright. All rights reserved.

Author Manuscript

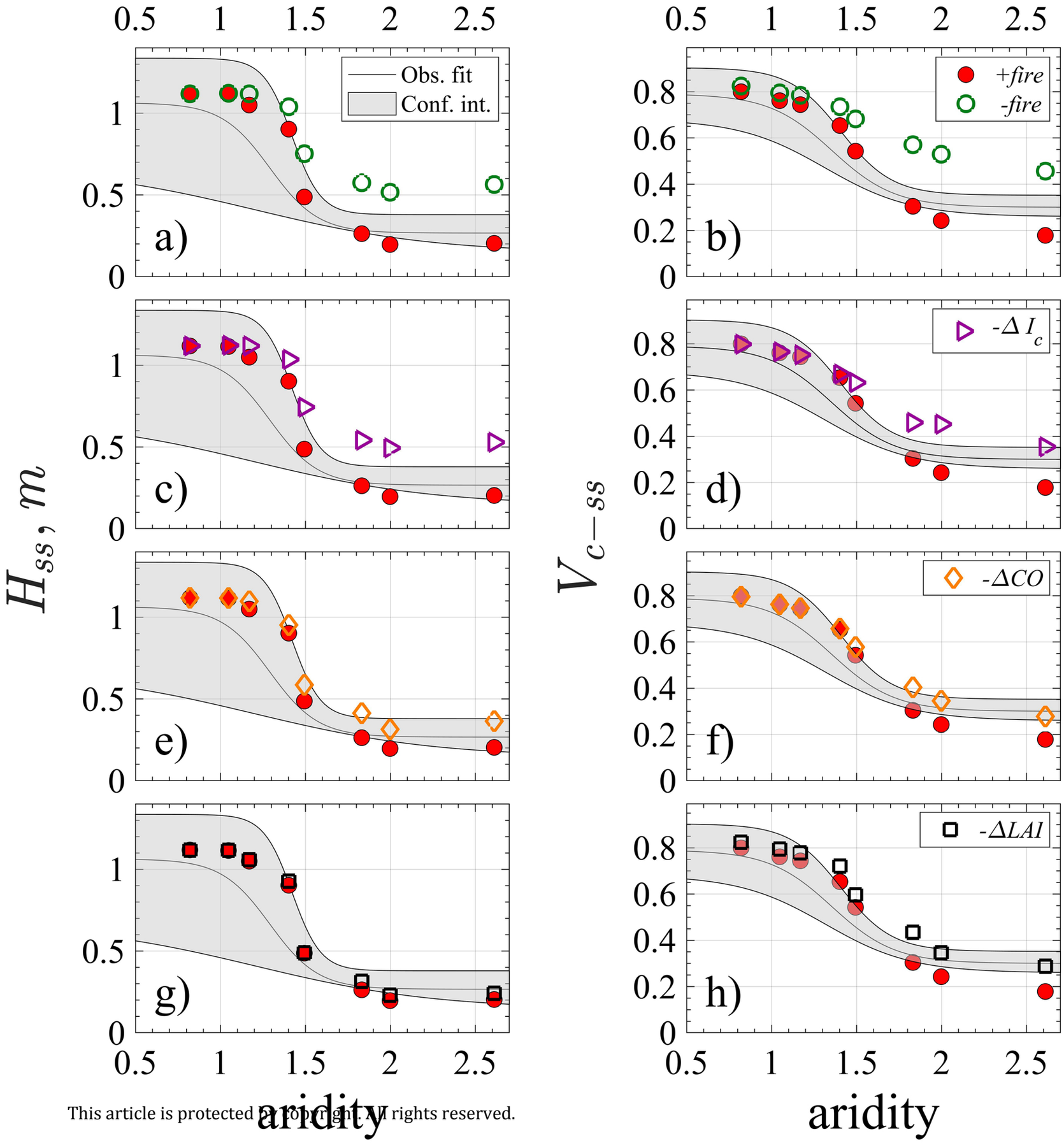

This article is protected by copyright. All rights reserved.

Author Manuscript

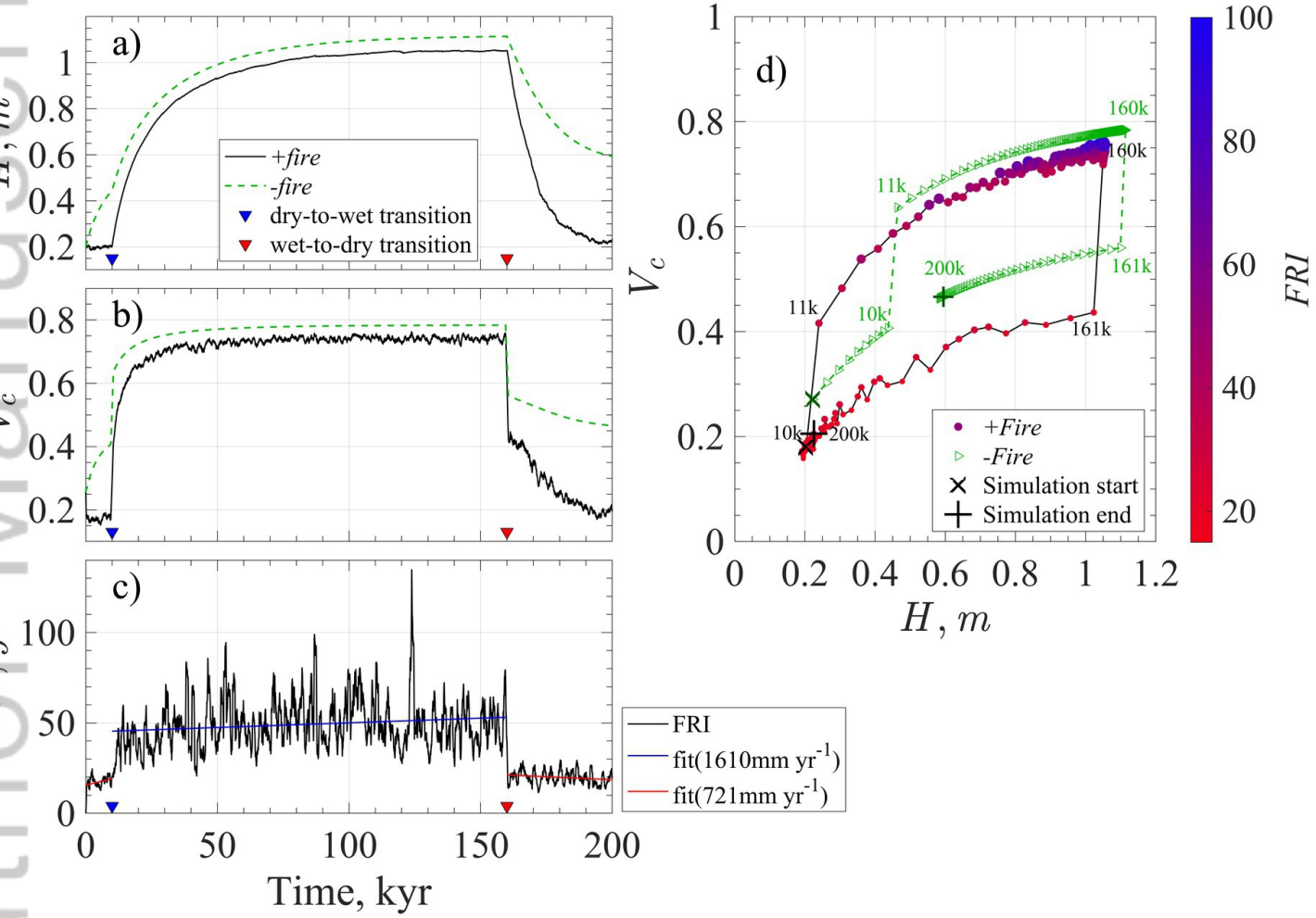

2019WR026005-f08-z-.jpg

This article is protected by copyright. All rights reserved.

Author Manuscript

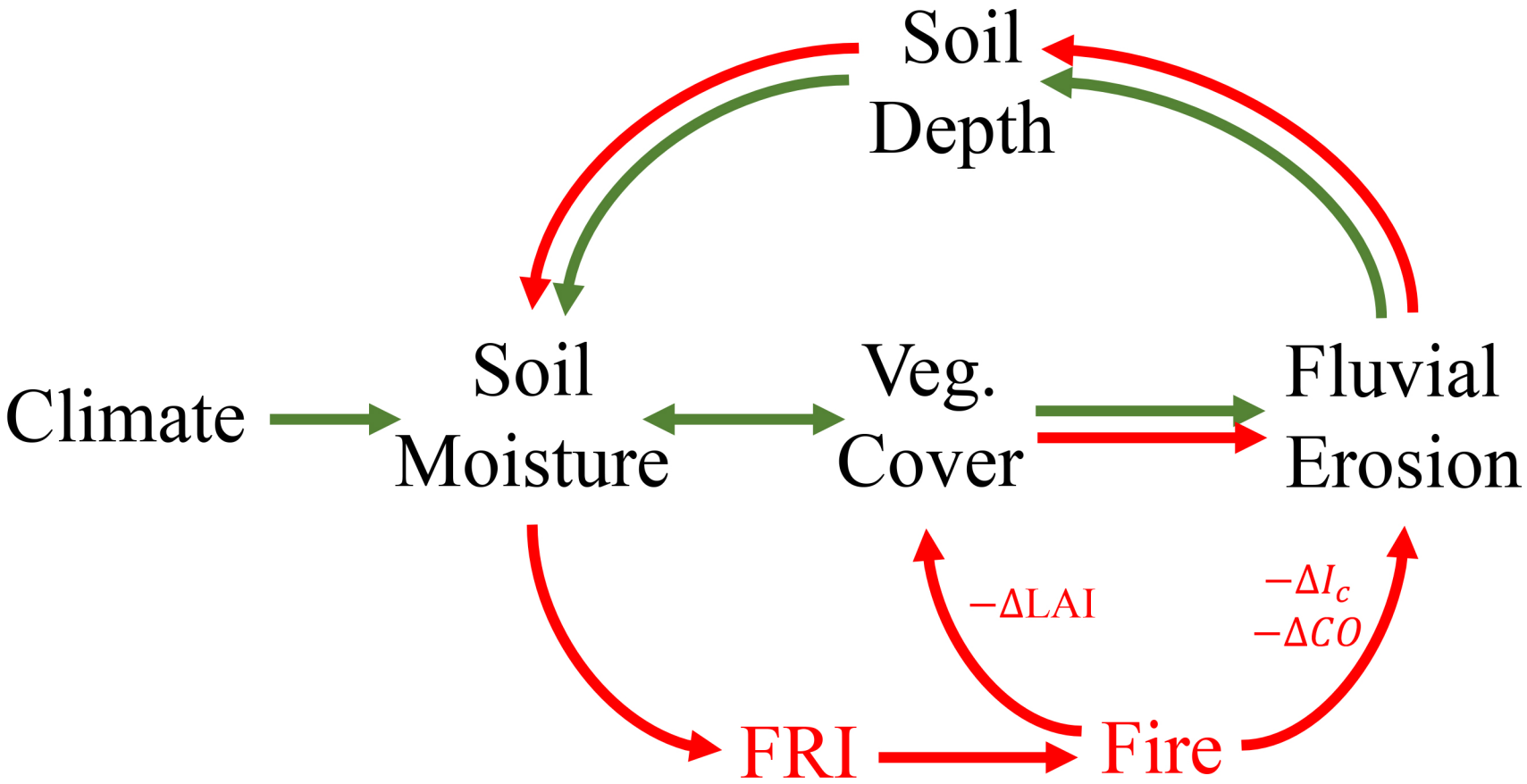

This article is protected by copyright. All rights reserved.